Commun. Comput. Phys.
doi: 10.4208/cicp.130313.210613s

Vol. **15**, No. 4, pp. 911-943
April 2014

# A High-Order Accurate Gas-Kinetic Scheme for One- and Two-Dimensional Flow Simulation

Na Liu[†] and Huazhong Tang[*]

*HEDPS, CAPT & LMAM, School of Mathematical Sciences, Peking University, Beijing 100871, P.R. China.*

Received 13 March 2013; Accepted (in revised version) 21 June 2013

Available online 21 January 2014

**Abstract.** This paper develops a high-order accurate gas-kinetic scheme in the framework of the finite volume method for the one- and two-dimensional flow simulations, which is an extension of the third-order accurate gas-kinetic scheme [*Q.B. Li, K. Xu, and S. Fu, J. Comput. Phys., 229(2010), 6715-6731*] and the second-order accurate gas-kinetic scheme [*K. Xu, J. Comput. Phys., 171(2001), 289-335*]. It is formed by two parts: quartic polynomial reconstruction of the macroscopic variables and fourth-order accurate flux evolution. The first part reconstructs a piecewise cell-center based quartic polynomial and a cell-vertex based quartic polynomial according to the "initial" cell average approximation of macroscopic variables to recover locally the non-equilibrium and equilibrium single particle velocity distribution functions around the cell interface. It is in view of the fact that all macroscopic variables become moments of a single particle velocity distribution function in the gas-kinetic theory. The generalized moment limiter is employed there to suppress the possible numerical oscillation. In the second part, the macroscopic flux at the cell interface is evolved in fourth-order accuracy by means of the simple particle transport mechanism in the microscopic level, i.e. free transport and the Bhatnagar-Gross-Krook (BGK) collisions. In other words, the fourth-order flux evolution is based on the solution (i.e. the particle velocity distribution function) of the BGK model for the Boltzmann equation. Several 1D and 2D test problems are numerically solved by using the proposed high-order accurate gas-kinetic scheme. By comparing with the exact solutions or the numerical solutions obtained the second-order or third-order accurate gas-kinetic scheme, the computations demonstrate that our scheme is effective and accurate for simulating invisid and viscous fluid flows, and the accuracy of the high-order `GKS` depends on the choice of the (numerical) collision time.

**AMS subject classifications**: 76M12, 76M25, 76N15

**Key words**: Gas-kinetic scheme, initial reconstruction, BGK model, Boltzmann equation, velocity distribution function.

[†]Address correspondence to Dr. Na Liu: High Performance Simulation Software Center, China Academy of Engineering Physics, Beijing 100088, P.R. China.
[*]Corresponding author. *Email addresses:* `nliu@pku.edu.cn` (N. Liu), `hztang@math.pku.edu.cn` (H. Z. Tang)

 ©2014 Global-Science Press

# 1 Introduction

Over the past three decades there have been many research activities in the design and application of high order accurate numerical methods in computational fluid dynamics. High order methods are especially desirable for simulating flows with complicated solution structures. Up to now, based on the idea of Godunov method [3], many people developed various schemes based on approximate Riemann solver and various high-order accurate Godunov-type schemes and applied to some practical problems successfully. Some examples are MUSCL (monotone upstream-centered schemes for conservation laws) scheme [28], the total variation diminishing scheme [6], the essential non-oscillatory method scheme [7], the weighted essential non-oscillatory method scheme [16], the discontinuous Galerkin method [2], the spectral difference (SD) method [17], and spectral volume method (SV) [30] and so on. Upwind and high-resolution methods are well-reviewed in [29] and the high-ordered WENO schemes are summed up in [19]. We also refer the readers to the books [2, 14, 27] and references therein.

The aim of this paper is to construct a high-order accurate gas-kinetic scheme for one- and two-dimensional flow simulations from the viewpoint of gas-kinetic theory. The development of the gas-kinetic schemes including the KFVS [18] and BGK-type scheme [34] for compressible flow simulations has attracted much attention in the past two decade years. The gas-kinetic BGK schemes is a class of finite volume schemes to evolve the macroscopic variables and are constructed based on the solution of the Bhatnagar-Gross-Krook (BGK) model of Boltzmann or collisionless Boltzmann equation. It turns out that the gas-kinetic schemes have provided robust and accurate numerical solutions for various unsteady compressible flows, see [22–24] and references therein. Some theoretical analysis has also been carried out for the gas-kinetic schemes, see e.g. [25, 26], etc. Recently, a third order gas-kinetic Navier-Stokes solver with one dimensional flux evaluation has been presented in [15].

The paper is organized as follows. Section 2 introduces the BGK model. Section 3 presents our high-order accurate gas-kinetic scheme including two quartic polynomial reconstructions of the macroscopic variables and fourth-order accurate flux evolution. The generalized moment limiter is also implemented detailedly. Several 1D and 2D test problems are solved in Section 4 to demonstrate the effectiveness and accuracy of our proposed scheme in simulating invisid and viscous fluid flows. Conclusion is given in Section 5.

# 2 The BGK model

In physics, specifically non-equilibrium statistical mechanics, the Boltzmann equation or Boltzmann transport equation describes the statistical behaviour of a fluid not in thermodynamic equilibrium, i.e. when there are temperature gradients in space causing heat to flow from hotter regions to colder ones, by the random (and biased) transport of parti-

cles. The starting point of the gas-kinetic schemes [15,33,34] is the the BGK model (2.1) of the Boltzmann equation as well as its analytic solution. Assume that there is no any force field acting on the particles in the fluid. The one-dimensional Bhatnagar-Gross-Krook (BGK) model can be written as [10]

$$f_t+uf_x=\frac{g-f}{\tau}, \tag{2.1}$$

where $f$ is the particle velocity distribution function and $g$ is corresponding equilibrium distribution. Both $f$ and $g$ are functions of space $x$, time $t$, the particle velocity $u$ in $x$-direction, and the internal variables $\boldsymbol{\xi}=(\xi_1,\xi_2,\cdots,\xi_K)$, which has $K$ degrees of freedom. The total number of degree of freedom $K$ is related to the ratio of specific heats $\gamma$ by $K=2/(\gamma-1)-d$, where $d$ denotes the spatial dimension. For example, for a diatomic gas with $\gamma=7/5$ in 2D space, $K$ is equal to 3 to account for the particle motion in the $z$-direction and two rotational degrees of freedom. The equilibrium distribution function $g$ is the Maxwellian

$$g=\rho\left(\frac{\lambda}{\pi}\right)^{\frac{K+1}{2}}e^{-\lambda\left((u-U)^2+\xi^2\right)}, \tag{2.2}$$

where $\rho$ is the fluid density, $U$ is the fluid velocity, $\lambda$ is equal to $m/2kT$, here $m$ is the fluid molecular mass, $k$ is the Boltzmann constant, and $T$ is the fluid temperature. In the equilibrium state, the internal variable $\xi^2$ is equal to $\xi^2=\xi_1^2+\xi_2^2+\ldots+\xi_K^2$. The particle collision time $\tau$ is related to the fluid viscosity by $\tau=\mu/P$, where $\mu$ is the dynamical viscosity and $P$ is the fluid pressure.

The analytic solution of the BGK model (2.1) may be derived as follows

$$f(x,t,u,\boldsymbol{\xi})=\frac{1}{\tau}\int_0^t g(x',t',u,\boldsymbol{\xi})e^{-(t-t')/\tau}dt'+e^{-t/\tau}f_0(x-ut,u,\boldsymbol{\xi}), \tag{2.3}$$

where $x'=x-u(t-t')$ is the particle trajectory, and $f_0$ is the initial particle velocity distribution function, i.e. $f(x,0,u,\boldsymbol{\xi})=f_0(x,u,\boldsymbol{\xi})$.

In the gas-kinetic representation, all macroscopic flow variables become moments of a single particle velocity distribution function. In other words, the macroscopic variables, such as the density $\rho$, the momentum $\rho U$ and the total energy $E$ may relate to the velocity distribution function $f$ by means of the following moments

$$\boldsymbol{W}:=\begin{pmatrix}\rho\\ \rho U\\ E\end{pmatrix}=\int_{\mathbb{R}^{K+1}}\boldsymbol{\Psi}f\,dud\boldsymbol{\xi}, \tag{2.4}$$

where $\boldsymbol{\Psi}$ is the moment vector

$$\boldsymbol{\Psi}=\left(1,u,\frac{1}{2}(u^2+\xi^2)\right)^T,$$

and $d\boldsymbol{\xi}=d\xi_1 d\xi_2\cdots d\xi_K$. During the particle collisions, $f$ and $g$ satisfy the conservation constraints

$$\int_{\mathbb{R}^{K+1}} \boldsymbol{\Psi}(g-f)\,du d\boldsymbol{\xi}=0, \tag{2.5}$$

at any point in space and time, which imply the mass, momentum, and energy conservations.

The macroscopic equations governing the fluid flows may be derived from the Boltzmann equation or the BGK model by using the Chapman-Enskog expansion. For example, for a local equilibrium state with $f=g$, the Euler equations can be obtained by taking the moments of (2.1)

$$\begin{pmatrix}\rho\\ \rho U\\ E\end{pmatrix}_t+\begin{pmatrix}\rho U\\ \rho U^2+P\\ (E+P)U\end{pmatrix}_x=0, \tag{2.6}$$

where $E=\frac{1}{2}\rho(U^2+\frac{K+d}{2\lambda})$ and $P=\rho/2\lambda$. To the first order of $\tau$, the Chapman-Enskog expansion gives

$$f=g-\tau(g_t+ug_x)=:g\big(1-\tau(A+au)\big). \tag{2.7}$$

Substituting this expansion of $f$ to the BGK equation (2.1), and taking its $\boldsymbol{\Psi}$ moments derive the Navier-Stokes equations

$$\begin{pmatrix}\rho\\ \rho U\\ E\end{pmatrix}_t+\begin{pmatrix}\rho u\\ \rho U^2+P\\ (E+P)U\end{pmatrix}_x=\begin{pmatrix}0\\ \frac{2K}{K+1}\mu U_x\\ \frac{K+3}{4}\mu(\frac{1}{\lambda})_x+\frac{2K}{K+1}\mu UU_x\end{pmatrix}_x, \tag{2.8}$$

with $\mu=\tau p$. The full derivation of the Navier-Stokes equations for a monatomic gas from the BGK model in 3D case may be similarly derived.

## 3 The numerical scheme

This section will introduce our high-order accurate gas-kinetic scheme, which is an extension of the existing gas-kinetic schemes, see e.g. [15,34].

For the sake of simplicity, the computational domain $\Omega$ is divided into a mesh $\{I_j=(x_{j-\frac{1}{2}},x_{j+\frac{1}{2}})\subset\Omega, j\in\mathbb{Z}\}$, the length of the cell $I_j$ is denoted by $h_j:=x_{j+\frac{1}{2}}-x_{j-\frac{1}{2}}$. The time domain $[0,T]$ is also divided into a (non-uniform) mesh $\{t_{n+1}=t_n+\Delta t_n,\ t_0=0,\ n\geq 0\}$ with the time step size $\Delta t_n$ determined by

$$\Delta t_n=\frac{Ch_j}{\max_j\{|\overline{U}_j|+\bar{c}_j\}}, \tag{3.1}$$

where the constant $C$ denotes the CFL number, $\overline{U}_j$ and $\bar{c}_j$ denote corresponding cell average approximations of the velocity $U$ and the speed of sound $c=\sqrt{(\partial p/\partial\rho)_S}$ over the

cell $I_j$. Here $(\partial p/\partial\rho)_S$ denotes the partial derivative of the pressure with respect to the density taken adiabatically, that is, at constant entropy per particle.

Taking the moments of the BGK equation (2.1) and integrating them over $I_j\times[t_n,t_{n+1})$, i.e.

$$\int_{t_n}^{t_{n+1}}\int_{I_j}\int_{\mathbb{R}^{K+1}}\boldsymbol{\Psi}\left(f_t+uf_x-\frac{1}{\tau}(g-f)\right)\,dud\boldsymbol{\xi}dxdt=0.$$

With the help of the conservation constraints (2.5), one has

$$\begin{aligned}&\int_{I_j}\int_{\mathbb{R}^{K+1}}\boldsymbol{\Psi}f(x,t_{n+1},u,\boldsymbol{\xi})\,dud\boldsymbol{\xi}dx\\&=\int_{I_j}\int_{\mathbb{R}^{K+1}}\boldsymbol{\Psi}f(x,t_n,u,\boldsymbol{\xi})\,dud\boldsymbol{\xi}dx-\int_{t_n}^{t_{n+1}}\int_{\mathbb{R}^{K+1}}\boldsymbol{\Psi}u\left(f(x_{j+\frac{1}{2}},t,u,\boldsymbol{\xi})-f(x_{j-\frac{1}{2}},t,u,\boldsymbol{\xi})\right)\,dud\boldsymbol{\xi}dt.\end{aligned}$$

From that, one may derive the 1D gas-kinetic scheme in the following conservative form

$$\overline{\boldsymbol{W}}_j^{n+1}=\overline{\boldsymbol{W}}_j^n-\frac{\Delta t_n}{h_j}\left(\widehat{\boldsymbol{F}}_{j+\frac{1}{2}}^n-\widehat{\boldsymbol{F}}_{j-\frac{1}{2}}^n\right),\tag{3.2}$$

where $\overline{\boldsymbol{W}}_j^n$ is the cell-average approximation of the solution vector $\boldsymbol{W}(x,t_n)$ as follows

$$\overline{\boldsymbol{W}}_j^n\approx\frac{1}{h_j}\int_{I_j}\boldsymbol{W}(x,t_n)\,dx,$$

and

$$\widehat{\boldsymbol{F}}_{j+\frac{1}{2}}^n:=\frac{1}{\Delta t_n}\int_{\mathbb{R}^{K+1}}\boldsymbol{\Psi}u\int_{t_n}^{t_{n+1}}\hat{f}(x_{j+\frac{1}{2}},t,u,\boldsymbol{\xi})\,dtdud\boldsymbol{\xi}.\tag{3.3}$$

Here, $\hat{f}(x_{j+\frac{1}{2}},t,u,\boldsymbol{\xi})$ approximates $f(x_{j+\frac{1}{2}},t,u,\boldsymbol{\xi})$ given in (2.3).

The remaining task of finishing the gas-kinetic scheme is to suitably give $\hat{f}(x_{j+\frac{1}{2}},t,u,\boldsymbol{\xi})$ by means of the initial reconstruction of the macroscopic variables $\boldsymbol{W}$.

### 3.1 Initial data reconstruction

From the given "initial data" $\{\overline{\boldsymbol{W}}_j^n\}$, we first reconstruct a cell-center based piecewise quartic polynomial

$$\boldsymbol{W}_h^n(x)=\sum_{\ell=0}^{4}\overline{\boldsymbol{W}}_j^{n,(\ell)}\phi^{(\ell)}(x-x_j)=:\boldsymbol{W}_j^n(x),\quad x\in I_j,\tag{3.4}$$

where $x_j$ represents the cell centroid coordinate and

$$\begin{aligned}
&\phi^{(0)}(\tilde{x})=1,\\
&\phi^{(1)}(\tilde{x})=\tilde{x},\\
&\phi^{(2)}(\tilde{x})=\frac{1}{2!}\tilde{x}^2-\frac{1}{4!}h_j^2,\\
&\phi^{(3)}(\tilde{x})=\frac{1}{3!}\tilde{x}^3-\frac{1}{4!}h_j^2\tilde{x},\\
&\phi^{(4)}(\tilde{x})=\frac{1}{4!}\tilde{x}^4-\frac{1}{2\times 4!}h_j^2\tilde{x}^2+\frac{7}{24\times 6!}h_j^4.
\end{aligned}$$

The cell-averaged derivatives $\overline{W}_j^{n,(\ell)}$, $\ell=0,1,2,3,4$, are obtained by the requirement of the mass, momentum, and energy conservations over the neighboring cells as follows

$$\sum_{\ell=0}^{4}\overline{W}_j^{n,(\ell)}\int_{I_m}\phi^{(\ell)}(x-x_j)\,dx=\int_{I_m}W_j^n(x)\,dx=h_m\overline{W}_m^n,\quad m=j,j\pm1,j\pm2. \tag{3.5}$$

For example, if the mesh is uniform, i.e. $h_j=h$ for each cell $I_j$, then the solutions of the linear algebraic system (3.5) are

$$\begin{aligned}
&\overline{W}_j^{n,(0)}=\overline{W}_j^n,\\
&\overline{W}_j^{n,(1)}=\frac{1}{12h}\left(\overline{W}_{j-2}^n-8\overline{W}_{j-1}^n+8\overline{W}_{j+1}^n-\overline{W}_{j+2}^n\right),\\
&\overline{W}_j^{n,(2)}=\frac{1}{12h^2}\left(-\overline{W}_{j-2}^n+16\overline{W}_{j-1}^n-30\overline{W}_j^n+16\overline{W}_{j+1}^n-\overline{W}_{j+2}^n\right),\\
&\overline{W}_j^{n,(3)}=\frac{1}{2h^3}\left(-\overline{W}_{j-2}^n+2\overline{W}_{j-1}^n-2\overline{W}_{j+1}^n+\overline{W}_{j+2}^n\right),\\
&\overline{W}_j^{n,(4)}=\frac{1}{h^4}\left(\overline{W}_{j-2}^n-4\overline{W}_{j-1}^n+6\overline{W}_j^n-4\overline{W}_{j+1}^n+\overline{W}_{j+2}^n\right).
\end{aligned}$$

The above reconstruction (3.4) will generate significant oscillations and even nonlinear instability when the solutions $\boldsymbol{W}$ contain large gradient or discontinuity. To avoid such difficulties, we have to borrow a technique of a slope limiter to limit the cell-averaged derivatives of $W_h^n(x)$ in (3.4). Such limiting procedure must be designed to control spurious oscillations and at the same time maintain accuracy in smooth regions in a robust way. Here we adopt the generalized moment limiter [1,11,35], in which the cell-averaged derivatives $\{\overline{W}_j^{n,(\ell)},1\le\ell\le4\}$ are hierarchically limited in two stages. The first stage of the present generalized moment limiter is to identify whether the cell-averaged derivatives $\{\overline{W}_j^{n,(\ell)},1\le\ell\le4\}$ is necessarily limited in a componentwise way. For this purpose, we introduce a new variables $P_j^{(\ell)}$ with the initial value of 1 to mark whether or not $\overline{W}_j^{n,(\ell)}$ is

necessarily limited, $\ell \geq 1$. The detailed implementation of this stage is as follows

```
do j=1,2,⋯,J
    do ℓ=4,3,2,1
        W̃_j^{n,(ℓ)} := m( W̄_j^{n,(ℓ)}, β (W̄_{j+1}^{n,(ℓ-1)} − W̄_j^{n,(ℓ-1)}) / (½(h_j+h_{j+1})), β (W̄_j^{n,(ℓ-1)} − W̄_{j-1}^{n,(ℓ-1)}) / (½(h_j+h_{j-1})) )
        if W̃_j^{n,(ℓ)} = W̄_j^{n,(ℓ)}
            do m=ℓ−1,⋯,1
                W̃_j^{n,(m)} = W̄_j^{n,(m)}
            enddo
            goto 100
        else
            P_j^{(ℓ)} = 0
        endif
    enddo
100 continue
enddo
```

where $J$ denotes the total number of cells, $m(a,b,c)$ denotes the minmod function, defined by

$$m(a,b,c) = \begin{cases} s\cdot\min\{|a|,|b|,|c|\}, & \text{if } \operatorname{sign}(a)=\operatorname{sign}(a)=\operatorname{sign}(c)=:s, \\ 0, & \text{otherwise,} \end{cases}$$

which is applied to each component of the vector $\boldsymbol{W}$, even though we write them in a vector form. The value of $\beta$ is taken as 1.5 in our computations.

The second stage of the present generalized moment limiter starts to limit the cell-averaged derivatives $\{\overline{W}_j^{n,(\ell)}, 1 \leq \ell \leq 4\}$ component-wisely according to the value of $\boldsymbol{P}_j^{(\ell)}$. It is implemented as follows

```
do ℓ=1,2,3
    do j=1,2,⋯,J
        if P_{j-1}^{(ℓ)} P_j^{(ℓ)} P_{j+1}^{(ℓ)} = 0
            W̃_j^{n,(ℓ+1)} := m( W̄_j^{n,(ℓ+1)}, β (W̃_{j+1}^{n,(ℓ)} − W̃_j^{n,(ℓ)}) / (½(h_j+h_{j+1})), β (W̃_j^{n,(ℓ)} − W̃_{j-1}^{n,(ℓ)}) / (½(h_j+h_{j-1})) )
```

if $\widetilde{W}_j^{n,(\ell+1)} \neq \overline{W}_j^{n,(\ell+1)}$, then $P_j^{(\ell+1)} = 0$

endif

enddo

enddo

After using the above limiting procedure for the cell-averaged derivatives $\{\overline{W}_j^{n,(\ell)}, 0 \leq \ell \leq 4\}$, the reconstructed polynomials $W_j^n(x)$ in (3.4) are replaced with

$$\widetilde{W}_j^n(x) = \overline{W}_j^n + \widetilde{W}_j^{n,(1)}(x-x_j) + \frac{1}{2}\widetilde{W}_j^{n,(2)}\Big((x-x_j)^2 - \frac{1}{12}h_j^2\Big) + \frac{1}{6}\widetilde{W}_j^{n,(3)}\Big((x-x_j)^3 - \frac{1}{4}h_j^2(x-x_j)\Big) + \frac{1}{24}\widetilde{W}_j^{n,(4)}\Big((x-x_j)^4 - \frac{1}{2}h_j^2(x-x_j)^2 + \frac{7}{720}h_j^4\Big), \quad x \in I_j. \tag{3.6}$$

### 3.2 Fourth-order accurate flux evolution

This section is to give the numerical flux $\widehat{F}_{j+\frac{1}{2}}^n$ in the gas-kinetic scheme (3.2), equivalently, to calculate $\hat{f}(x_{j+\frac{1}{2}},t,u,\xi)$ in (3.3) by using $\widetilde{W}_j^n(x)$ and the solution of the BGK model, i.e.

$$\hat{f}(x_{j+\frac{1}{2}},t,u,\xi) = \frac{1}{\tau}\int_0^t g_h(x',t',u,\xi)e^{-(t-t')/\tau}dt' + e^{-t/\tau}f_{h,0}(x_{j+\frac{1}{2}}-ut,u,\xi), \tag{3.7}$$

where $x' = x_{j+\frac{1}{2}} - u(t-t')$ is the particle trajectory past the point $(x_{j+\frac{1}{2}},t)$, and $f_{h,0}(x_{j+\frac{1}{2}} - ut,u,\xi)$ and $g_h(x',t',u,\xi)$ are corresponding (approximate) the initial velocity distribution and equilibrium velocity distribution functions, which are presented in Sections 3.2.1 and 3.2.2, respectively.

For the cell interface $x_{j+\frac{1}{2}}$, we have the following limiting values of $W_h(x,t_n)$ or its $\ell$th order derivative with respect to $x$

$$\begin{aligned}
&W_{j+\frac{1}{2},L}^n := W_h(x_{j+\frac{1}{2}}-0,t_n) \equiv \widetilde{W}_j^n(x_{j+\frac{1}{2}}),\\
&W_{j+\frac{1}{2},R}^n := W_h(x_{j+\frac{1}{2}}+0,t_n) \equiv \widetilde{W}_{j+1}^n(x_{j+\frac{1}{2}}),\\
&W_{j+\frac{1}{2},L}^{n,(\ell)} := \frac{d^\ell W_h}{dx^\ell}(x_{j+\frac{1}{2}}-0,t_n) \equiv \frac{d^\ell \widetilde{W}_j^n}{dx^\ell}(x_{j+\frac{1}{2}}),\\
&W_{j+\frac{1}{2},R}^{n,(\ell)} := \frac{d^\ell W_h}{dx^\ell}(x_{j+\frac{1}{2}}+0,t_n) \equiv \frac{d^\ell \widetilde{W}_{j+1}^n}{dx^\ell}(x_{j+\frac{1}{2}}).
\end{aligned} \tag{3.8}$$

By using $W_{j+\frac{1}{2},L}^n$ and $W_{j+\frac{1}{2},R}^n$ in (3.8), we define the left and right Maxwellian distribution

functions according to (2.2)

$$g_L := \rho^n_{j+\frac{1}{2},L}\left(\frac{\lambda^n_{j+\frac{1}{2},L}}{\pi}\right)^{\frac{K+1}{2}} e^{-\lambda\left((u-U^n_{j+\frac{1}{2},L})^2+\xi^2\right)},$$
$$g_R = \rho^n_{j+\frac{1}{2},R}\left(\frac{\lambda^n_{j+\frac{1}{2},R}}{\pi}\right)^{\frac{K+1}{2}} e^{-\lambda\left((u-U^n_{j+\frac{1}{2},R})^2+\xi^2\right)}, \tag{3.9}$$

and the macroscopic variables $\boldsymbol{W}$ at the cell interface $x_{j+\frac{1}{2}}$ by

$$\boldsymbol{W}^n_{j+\frac{1}{2}} := \int_{u>0}\int_{\mathbb{R}^K} \boldsymbol{\Psi} g_L \, du d\boldsymbol{\xi} + \int_{u<0}\int_{\mathbb{R}^K} \boldsymbol{\Psi} g_R \, du d\boldsymbol{\xi}, \tag{3.10}$$

from which, according to (2.2), the Maxwellian distribution function is defined at cell interface $x_{j+\frac{1}{2}}$ and $t=t_n$ may be defined by

$$g_0 := \rho^n_{j+\frac{1}{2}}\left(\frac{\lambda^n_{j+\frac{1}{2}}}{\pi}\right)^{\frac{K+1}{2}} e^{-\lambda\left((u-U^n_{j+\frac{1}{2}})^2+\xi^2\right)}.$$

In the following, we will derive the initial velocity distribution function $f_{h,0}(x,u,\xi)$ and the equilibrium velocity distribution $g_h(x,t,u,\boldsymbol{\xi})$, separately.

### 3.2.1 Initial velocity distribution function $f_{h,0}$

This section will borrow the first-order Chapman-Enskog expansion (2.7), i.e.

$$f(x,t,u,\boldsymbol{\xi}) = g(x,t,u,\boldsymbol{\xi})\Big(1-\tau\big(a(x,t,u,\boldsymbol{\xi})u+A(x,t,u,\boldsymbol{\xi})\big)\Big), \tag{3.11}$$

to give the initial velocity distribution function $f_{h,0}$. Here we always assume that $f$ and $g$ are sufficiently smooth. Due to the conservation constraints (2.5), the Chapman-Enskog expansion (3.11) implies

$$\int_{\mathbb{R}^{K+1}} \boldsymbol{\Psi}(au+A)g \, du d\xi = \int_{\mathbb{R}^{K+1}} \boldsymbol{\Psi}(g_t+ug_x) du d\boldsymbol{\xi} \equiv \frac{1}{\tau}\int_{\mathbb{R}^{K+1}} \boldsymbol{\Psi}(g-f) du d\boldsymbol{\xi} = 0, \tag{3.12}$$

and

$$\begin{aligned}
&\int_{\mathbb{R}^{K+1}} \boldsymbol{\Psi}(C+aA+(b+a^2)u)g\ dud\xi = \int_{\mathbb{R}^{K+1}} \boldsymbol{\Psi}(g_{xt}+ug_{xx})\ dud\xi = 0,\\
&\int_{\mathbb{R}^{K+1}} \boldsymbol{\Psi}(A^2+B+(Aa+C)u)g\ dud\xi = \int_{\mathbb{R}^{K+1}} \boldsymbol{\Psi}(g_{tt}+ug_{xt})\ dud\xi = 0,\\
&\int_{\mathbb{R}^{K+1}} \boldsymbol{\Psi}(D+2aC+Ab+Aa^2+(a^3+3ab+d)u)g\ dud\xi = \int_{\mathbb{R}^{K+1}} \boldsymbol{\Psi}(g_{xxt}+ug_{xxx})\ dud\xi = 0,\\
&\int_{\mathbb{R}^{K+1}} \boldsymbol{\Psi}(A^3+3AB+\widetilde{B}+(A^2a+Ba+2AC+\overline{B})u)g\ dud\xi = \int_{\mathbb{R}^{K+1}} \boldsymbol{\Psi}(g_{ttt}+ug_{xtt})\ dud\xi = 0,\\
&\int_{\mathbb{R}^{K+1}} \boldsymbol{\Psi}(\overline{B}+2AC+aB+aA^2+(Aa^2+Ab+2aC+D)u)g\ dud\xi\\
&\quad = \int_{\mathbb{R}^{K+1}} \boldsymbol{\Psi}(g_{xtt}+ug_{xxt})\ dud\xi = 0,
\end{aligned} \tag{3.13}$$

and so on, where $b=\partial a/\partial x$, $C=\partial A/\partial x$, $D=\partial C/\partial x$, $d=\partial b/\partial x$, $B=\partial A/\partial t$, $\overline{B}=\partial B/\partial x$, and $\widetilde{B}=\partial B/\partial t$.

Using (3.11) and Taylor's expansion of any sufficiently smooth function $w(x)$ at $x_{j+\frac{1}{2}}$

$$w(x)=w(x_{j+\frac{1}{2}})+\frac{\partial w}{\partial x}(x_{j+\frac{1}{2}})\tilde{x}+\frac{1}{2}\frac{\partial^2 w}{\partial x^2}(x_{j+\frac{1}{2}})\tilde{x}^2+\frac{1}{6}\frac{\partial^3 w}{\partial x^3}(x_{j+\frac{1}{2}})\tilde{x}^3+\cdots,$$

where $\tilde{x}=x-x_{j+\frac{1}{2}}$, we give the approximate initial velocity distribution function $f_{h,0}:=f_{h,0}(x,u,\xi)$ around the cell interface $x_{j+\frac{1}{2}}$ as follows

$$f_{h,0}=\begin{cases}
g_L\big[1-\tau(a_Lu+A_L)+a_L\tilde{x}-\tau(C_L+A_La_L)\tilde{x}\\
+(b_L+a_L^2)(\frac{1}{2}\tilde{x}^2-\tau u\tilde{x})-\frac{1}{2}\tilde{x}^2\tau(D_L+2C_La_L+A_Lb_L+A_La_L^2)\\
+(d_L+3a_Lb_L+a_L^3)(\frac{1}{6}\tilde{x}^3-\frac{1}{2}\tilde{x}^2\tau u)\big], & \tilde{x}<0,\\
g_R\big[1-\tau(a_Ru+A_R)+a_R\tilde{x}-\tau(C_R+A_Ra_R)\tilde{x}\\
+(b_R+a_R^2)(\frac{1}{2}\tilde{x}^2-\tau u\tilde{x})-\frac{1}{2}\tilde{x}^2\tau(D_R+2C_Ra_R+A_Rb_R+A_Ra_R^2)\\
+(d_R+3a_Rb_R+a_R^3)(\frac{1}{6}\tilde{x}^3-\frac{1}{2}\tilde{x}^2\tau u)\big], & \tilde{x}>0,
\end{cases} \tag{3.14}$$

where $g_L$ and $g_R$ are given in (3.9), and $(a_L,A_L,C_L,b_L,D_L,d_L)$ and $(a_R,A_R,C_R,b_R,D_R,d_R)$ denote the left and right limits of $(a,A,C,b,D,d)$ at the cell interface $x_{j+\frac{1}{2}}$, respectively, and they are of the following form

$$w_L=w_{L,1}+w_{L,2}u+w_{L,3}\frac{1}{2}(u^2+\xi^2),\quad w=a,A,C,b,D,\text{ or } d.$$

Using the conservation constraints (3.12) at $t=t_n$ and the relationships between the velocity distribution function and the macroscopic variables:

$$\frac{d^\ell}{dx^\ell}\int_{\mathbb{R}^{K+1}} \boldsymbol{\Psi} f_{h,0}(x)dud\boldsymbol{\xi}=\frac{d^\ell}{dx^\ell}\widetilde{\mathbf{W}}_j^n(x),\quad \ell=1,2,3,$$

we may derive the linear systems for $a_L$,$b_L$,$d_L$ and $a_R$,$b_R$,$d_R$

$$\begin{aligned}
&<a_L>=\boldsymbol{W}^{n,(1)}_{j+\frac{1}{2},L}, && <a_R>=\boldsymbol{W}^{n,(1)}_{j+\frac{1}{2},R},\\
&<a_L^2+b_L>=\boldsymbol{W}^{n,(2)}_{j+\frac{1}{2},L}, && <a_R^2+b_R>=\boldsymbol{W}^{n,(1)}_{j+\frac{1}{2},R},\\
&<a_L^3+3a_Lb_L+d_L>=\boldsymbol{W}^{n,(3)}_{j+\frac{1}{2},L}, && <a_R^3+3a_Rb_R+d_R>=\boldsymbol{W}^{n,(3)}_{j+\frac{1}{2},R},
\end{aligned} \tag{3.15}$$

where

$$<\tilde{a}_L>=\int_{\mathbb{R}^{K+1}}\tilde{a}_Lg_L\boldsymbol{\Psi}\,dud\xi, \qquad <\tilde{a}_R>=\int_{\mathbb{R}^{K+1}}\tilde{a}_Rg_R\boldsymbol{\Psi}\,dud\xi,$$

for $\tilde{a}=a$, $a^2+b$, $a^3+3ab+d$. The first and second linear systems for $a_L$ and $a_R$ in (3.15) have the following form

$$\boldsymbol{M}\boldsymbol{w}=\boldsymbol{b}, \quad \boldsymbol{w}=a_L \text{ or } a_R, \tag{3.16}$$

with the coefficient matrix $\boldsymbol{M}$ given by

$$\boldsymbol{M}=\int_{\mathbb{R}^{K+1}}\boldsymbol{\Psi}^T\boldsymbol{\Psi}g\,dud\boldsymbol{\xi}/\rho=\begin{pmatrix} 1 & U & \frac{1}{2}U^2+\frac{K+1}{4\lambda}\\ U & U^2+\frac{1}{2\lambda} & \frac{1}{2}U^3+\frac{(K+3)U}{4\lambda}\\ \frac{1}{2}U^2+\frac{K+1}{4\lambda} & \frac{1}{2}U^3+\frac{(K+3)U}{4\lambda} & \frac{1}{4}U^4+\frac{(K+3)U^2}{4\lambda}+\frac{K^2+4K+3}{16\lambda^2}\end{pmatrix}.$$

Such linear system does also appear in the original BGK schemes, see [33,34]. By solving the first two linear systems in (3.15) to give $a_L$ and $a_R$, and then substituting them into the third and fourth linear systems in (3.15), one may get the linear systems for systems for $b_L$ and $b_R$ with the coefficient matrix $\boldsymbol{M}$. After that, substituting $a_L$,$b_L$,$a_R$,$b_R$ into the last two systems in (3.15) gives the linear systems for systems for $d_L$ and $d_R$ with the coefficient matrix $\boldsymbol{M}$.

Substituting $(a_L,b_L,a_R,b_R,d_L,d_R)$ into the conservation constraints (3.12) and (3.13) gives the linear systems for $A_L$, $A_R$, $C_L$, $C_R$, $D_L$ and $D_R$ as follows

$$\begin{aligned}
&<A_L+a_Lu>=0, \quad <A_R+a_Ru>=0,\\
&<C_L+a_LA_L+(a_L^2+b_L)u>=0, \quad <C_R+a_RA_R+(a_R^2+b_R)u>=0,\\
&<D_L+2a_LC_L+A_Lb_L+A_La_L^2+(a_L^3+3a_Lb_L+d_L)u>=0,\\
&<D_R+2a_RC_R+A_Rb_R+A_Ra_R^2+(a_R^3+3a_Rb_R+d_R)u>=0.
\end{aligned}$$

They are similar to the systems in (3.15) so that they may be solved in turn by using the same method or subroutine.

### 3.2.2 Equilibrium velocity distribution $g_h$

This section is to derive $g_h(x,t,u,\boldsymbol{\xi})$. First, using the "initial" cell average approximations of macroscopic variables $\{\overline{\boldsymbol{W}}_m, m=j-1,j,j+1,j+2\}$ as well as $\boldsymbol{W}^n_{j+\frac{1}{2}}=:\boldsymbol{W}_0$ defined by

(3.10), we reconstruct a cell-vertex based quartic polynomial around the cell interface $x_{j+\frac{1}{2}}$ as follows

$$W_0(x)=W_0+W_0^{(1)}\tilde{x}+\frac{1}{2}W_0^{(2)}\tilde{x}^2+\frac{1}{6}W_0^{(3)}\tilde{x}^3+\frac{1}{24}W_0^{(4)}\tilde{x}^4, \tag{3.17}$$

where coefficients $W_0^{(\ell)}$, $\ell=1,2,3,4$, are obtained by solving the algebraic system

$$\int_{I_m} W_0(x)\,dx=h_m\overline{W}_m, \quad m=j-1,j,j+1,j+2.$$

For example, if the mesh is uniform, i.e. $h_j=h$ for each cell $I_j$, then coefficients $W_0^{(\ell)}$, $\ell=1,2,3,4$, are

$$\begin{aligned}
W_0^{(1)}&=\frac{\overline{W}_{j-1}-15\overline{W}_j+15\overline{W}_{j+1}-\overline{W}_{j+2}}{12h},\\
W_0^{(2)}&=\frac{-\overline{W}_{j-1}+31\overline{W}_j+31\overline{W}_{j+1}-\overline{W}_{j+2}-60W_0}{8h^2},\\
W_0^{(3)}&=\frac{-\overline{W}_{j-1}+3\overline{W}_j-3\overline{W}_{j+1}+\overline{W}_{j+2}}{h^3},\\
W_0^{(4)}&=\frac{5(\overline{W}_{j-1}-7\overline{W}_j-7\overline{W}_{j+1}+\overline{W}_{j+2}+12W_0)}{2h^4}.
\end{aligned}$$

Then, borrowing Taylor's expansion of any sufficiently smooth function $w(x,t)$ at $(x_{j+\frac{1}{2}},t_n)$

$$\begin{aligned}
w(x,t)=&w(x_{j+\frac{1}{2}},t_n)+\frac{\partial w}{\partial x}(x_{j+\frac{1}{2}},t_n)\tilde{x}+\frac{\partial w}{\partial t}(x_{j+\frac{1}{2}},t_n)\tilde{t}+\frac{1}{2}\frac{\partial^2 w}{\partial x^2}(x_{j+\frac{1}{2}},t_n)\tilde{x}^2\\
&+\frac{1}{2}\frac{\partial^2 w}{\partial t^2}(x_{j+\frac{1}{2}},t_n)\tilde{t}^2+\frac{\partial^2 w}{\partial x\partial t}(x_{j+\frac{1}{2}},t_n)\tilde{x}\tilde{t}+\frac{1}{6}\frac{\partial^3 w}{\partial x^3}(x_{j+\frac{1}{2}},t_n)\tilde{x}^3+\frac{1}{2}\frac{\partial^3 w}{\partial x^2\partial t}(x_{j+\frac{1}{2}},t_n)\tilde{x}^2\tilde{t}\\
&+\frac{1}{2}\frac{\partial^3 w}{\partial x\partial t^2}(x_{j+\frac{1}{2}},t_n)\tilde{x}\tilde{t}^2+\frac{1}{6}\frac{\partial^3 w}{\partial t^3}(x_{j+\frac{1}{2}},t_n)\tilde{t}^3+\cdots,
\end{aligned}$$

where $\tilde{x}=x-x_{j+\frac{1}{2}}$, $\tilde{t}=t-t_n$, the equilibrium velocity distribution $g_h(x,t,u,\xi)$ in the small neighborhood of $(x_{j+\frac{1}{2}},t_n)$ can be constructed as follows

$$\begin{aligned}
g_h(x,t,u,\xi)=&g_0\Big[1+a_0\tilde{x}+A_0\tilde{t}+\frac{1}{2}(b_0+a_0^2)\tilde{x}^2+\frac{1}{2}(B_0+A_0^2)\tilde{t}^2+(C_0+A_0a_0)\tilde{x}\tilde{t}\\
&+\frac{1}{6}(d_0+3a_0b_0+a_0^3)\tilde{x}^3+\frac{1}{2}(D_0+2C_0a_0+A_0b_0+A_0a_0^2)\tilde{x}^2\tilde{t}\\
&+\frac{1}{2}(\overline{B}_0+B_0a_0+2A_0C_0+A_0^2a_0)\tilde{x}\tilde{t}^2+\frac{1}{6}(\widetilde{B}_0+3A_0B_0+A_0^3)\tilde{t}^3\Big],
\end{aligned} \tag{3.18}$$

where $(a_0,b_0,d_0,A_0,C_0,D_0,B_0,\overline{B}_0,\widetilde{B}_0)$ are the values of $(a,b,d,A,C,D,B,\overline{B},\widetilde{B})$ at the point $(x_{j+\frac{1}{2}},t_n)$.

By using the relationships between the velocity distribution function and the macroscopic variables

$$\left(\frac{d^\ell}{dx^\ell}\int_{\mathbb{R}^{K+1}}\Psi g_h(x,t_n,u,\xi)dud\boldsymbol{\xi}\right)_{x=x_{j+\frac{1}{2}}}=\left(\frac{d^\ell}{dx^\ell}\boldsymbol{W}_0(x)\right)_{x=x_{j+\frac{1}{2}}}\equiv\boldsymbol{W}_0^{(\ell)},\quad \ell=1,2,3,$$

we may get the linear systems for $a_0$, $b_0$ and $d_0$ as follows

$$\begin{aligned}
&<a_0>=\boldsymbol{W}_0^{(1)},\\
&<a_0^2+b_0>=\boldsymbol{W}_0^{(2)},\\
&<a_0^3+3a_0b_0+d_0>=\boldsymbol{W}_0^{(3)},
\end{aligned}\tag{3.19}$$

which are similar to the systems in (3.15) and may be solved in turn by using the same method or subroutine.

Substituting $(a_0,b_0,d_0)$ into the conservation constraints (3.12) and (3.13) gives the linear systems for $A_0$, $C_0$, $D_0$, $B_0$, $\overline{B}_0$, and $\widetilde{B}_0$ as follows

$$\begin{aligned}
&<A_0+a_0u>=0,\\
&<A_0a_0+C_0+(a_0^2+b_0)u>=0,\\
&<A_0^2+B_0+(A_0a_0+C_0)u>=0,\\
&<D_0+2a_0C_0+A_0b_0+A_0a_0^2+(a_0^3+3a_0b_0+d_0)u>=0,\\
&<\overline{B}_0+2A_0C_0+a_0B_0+a_0A_0^2+(A_0a_0^2+A_0b_0+2a_0C_0+D_0)u>=0,\\
&<A_0^3+3A_0B_0+\widetilde{B}_0+(A_0^2a_0+B_0a_0+2A_0C_0+\overline{B}_0)u>=0.
\end{aligned}$$

They are also similar to the systems in (3.15) so that they may be solved in turn by using the same method or subroutine. Until now, we complete the derivation of $g_h(x,t,u,\xi)$ in (3.18).

Next, substituting $f_{h,0}$ in (3.14) and $g_h$ in (3.18) into (3.7) gives the numerical velocity distribution function $\hat{f}(x_{j+\frac{1}{2}},t,u,\xi)$ at the cell interface $x=x_{j+\frac{1}{2}}$ as follows

$$\begin{aligned}
&\hat{f}(x_{j+\frac{1}{2}},t,u,\xi)\\
=&g_0\left[1+A_0\tilde{t}+\frac{1}{2}(B_0+A_0^2)\tilde{t}^2+\frac{1}{6}(\widetilde{B}_0+3A_0B_0+A_0^3)\tilde{t}^3\right]\\
&+e^{-\tilde{t}/\tau}\left\{f_{h,0}(x_{j+\frac{1}{2}}-u\tilde{t})-g_0\left[1-a_0u\tilde{t}+\frac{1}{2}(a_0^2+b_0)u^2\tilde{t}^2-\frac{1}{6}(a_0^3+3a_0b_0+d_0)u^3\tilde{t}^3\right]\right\}\\
&+(-\tau+\tau e^{-\tilde{t}/\tau})(A_0+a_0u)g_0-\tilde{t}\tau e^{-\tilde{t}/\tau}\left[A_0a_0+C_0+(a_0^2+b_0)u\right]ug_0\\
&-\tilde{t}\tau\left[A_0^2+B_0+(A_0a_0+C_0)u\right]g_0\\
&+\frac{1}{2}\tau\tilde{t}^2e^{-\tilde{t}/\tau}\left[D_0+2a_0C_0+A_0b_0+A_0a_0^2+(a_0^3+3a_0b_0+d_0)u\right]u^2g_0\\
&-\frac{1}{2}\tau\tilde{t}^2\left[A_0^3+3A_0B_0+\widetilde{B}_0+(A_0^2a_0+B_0a_0+2A_0C_0+\overline{B}_0)u\right]g_0.
\end{aligned}$$

It means that the numerical flux $\hat{F}^n_{j+\frac{1}{2}}$ may be obtained by inserting it into (3.3).

# 4 Numerical experiments

This section will solve several problems of the one- and two-dimensional fluid flow to demonstrate the accuracy and effectiveness of the gas-kinetic scheme proposed in the last section, compared with the schemes given in [15,34]. For the sake of convenience, we will use abbreviations "GKS2", "GKS3", and "GKS4" to denote the second-order accurate gas-kinetic scheme [34], the third-order accurate gas-kinetic scheme [15], and the present high-order accurate gas-kinetic schemes, respectively, and all physical quantities will be transformed as corresponding dimensionless variables by using the scaling parameters such as the characteristic length, the reference density, velocity, temperature and viscosity coefficient etc. Unless specifically stated, the specific heat ratio $\gamma$ is taken as 1.4 in all the cases, and the collision time $\tau$ at the cell interface is given by

$$\tau=\tau_m+C_2\triangle t_n^{\alpha}\frac{|P_L-P_R|}{|P_L+P_R|}, \tag{4.1}$$

with $\tau_m=\mu/P$ for the viscous flow and $\tau_m=C_1\triangle t_n^{\alpha}$ for the inviscid flow, $C_1$, $C_2$,and $\alpha$ are constants, $P_L$, $P_R$ are the left and right limit of the pressure at the cell interface, respectively. Unless specifically stated, we take $C_1=0.1$, $C_2=1$ and $\alpha=1$ in this section. In the literature, the parameter $\alpha$ is always equal to 1, see e.g. [15, 34] etc. Moreover, a Prandtl number fix will be adopted by modifying the energy flux [34] in the case of viscous flows if the Prandtl number is not equal to 1, because the BGK model is only recovering the Navier-Stokes equations with the Prandtl number of 1.

## 4.1 1D case

Three examples are considered here. The first one is to check the accuracy of the scheme and the followings are to validate the performance of GKS4 for strong shock structures. The time stepsize $\Delta t_n$ is determined by the $CFL$ condition (3.1) with the $CFL$ number of 0.2.

**Example 4.1** (Accuracy test)**.** This example is used to check the accuracy of GKS4 for smooth solutions. The initial conditions are taken as

$$\rho(x,0)=1+0.2\sin(\pi x),\quad U(x,0)=0.7,\quad P(x,0)=1.$$

The exact solution for this case is known

$$\rho(x,t)=1+0.2\sin\big(\pi(x-0.7t)\big),\quad U(x,t)=0.7,\quad P(x,t)=1,$$

which describes a sine wave propagating periodically in the domain $\Omega=[0,2]$.

Table 1: Example 4.1: Numerical errors (in $l^1$ norm) and convergence rates at $t=0.1$ for GKS4 as well as GKS3 with $\tau=0$.

| $N$ | GKS3 | | GKS4 | |
|---|---|---|---|---|
| | $l^1$ error | order | $l^1$ error | order |
| 10 | 1.57E-3 | —- | 2.85E-4 | — |
| 20 | 1.54E-4 | 3.35 | 1.34E-6 | 7.73 |
| 40 | 2.03E-5 | 2.92 | 4.24E-8 | 4.98 |
| 80 | 2.63E-6 | 2.95 | 1.33E-9 | 4.99 |
| 160 | 3.17E-7 | 3.05 | 4.21E-11 | 4.98 |
| 320 | 3.85E-8 | 3.04 | 1.31E-12 | 5.01 |
| 640 | 4.65E-9 | 3.05 | 4.11E-14 | 4.99 |

Table 2: Example 4.1: Numerical errors (in $l^1$ norm) and convergence rates at $t=0.1$ for GKS4 with $\alpha=4$ as well as GKS3 with $\alpha=3$.

| $N$ | GKS3 | | GKS4 | |
|---|---|---|---|---|
| | $\delta_N^1$ | $R_N^1$ | $\delta_N^1$ | $R_N^1$ |
| 10 | 7.56E-4 | —- | 3.98E-5 | — |
| 20 | 7.66E-5 | 3.30 | 1.30E-6 | 4.94 |
| 40 | 1.00E-5 | 2.94 | 4.10E-8 | 4.99 |
| 80 | 1.30E-6 | 2.94 | 1.29E-9 | 4.99 |
| 160 | 1.56E-7 | 3.06 | 4.07E-11 | 4.99 |
| 320 | 1.89E-8 | 3.05 | 1.27E-12 | 5.00 |
| 640 | 2.29E-9 | 3.04 | 3.98E-14 | 5.00 |

The domain $\Omega$ is divided into $N$ uniform cells and the periodic boundary conditions are specified at the end points $x=0$ and 2. Table 1 gives the $l^1$-errors at $t=0.1$ and corresponding convergence rates for GKS4 as well as GKS3 with $\tau=0$. It is found that the convergence rate of 5 order may be obtained for GKS4. Table 2 gives the $l^1$-errors at $t=0.1$ and corresponding convergence rates for GKS4 with $\alpha=4$ as well as GKS3 with $\alpha=3$, where $C_1=C_2=1$. It shows that the convergence rates of GKS4 and GKS3 is still about 5 and 3, respectively. Tables 3 and 4 further presents corresponding data for GKS4 (or GKS3) with $C_1=C_2=1$ and $\alpha=3$ (or 2) and 2 (or 1), respectively. Those results show that the accuracy of the high-order GKS depends on the (numerical) collision time $\tau$.

**Example 4.2** (Shock and sine wave interaction)**.** The example is first introduced by Shu and Osher in [20] for inviscid flow, which describes the interaction of a Mach 3 right-moving shock wave with a sine wave in density. It has widely been used to test the ability of the shock-capturing schemes in resolving small-scale flow features and may give a good indication of the numerical (artificial) viscosity of the scheme. The initial

Table 3: Example 4.1: Numerical errors (in $l^1$ norm) and convergence rates at $t=0.1$ for GKS4 with $\alpha=3$ as well as GKS3 with $\alpha=2$.

| $N$ | GKS3 | | GKS4 | |
|---|---|---|---|---|
| | $\delta_N^1$ | $R_N^1$ | $\delta_N^1$ | $R_N^1$ |
| 10 | 7.57E-4 | — | 3.98E-5 | — |
| 20 | 7.71E-5 | 3.30 | 1.30E-6 | 4.94 |
| 40 | 1.01E-5 | 2.93 | 4.13E-8 | 4.98 |
| 80 | 1.33E-6 | 2.92 | 1.33E-9 | 4.96 |
| 160 | 1.64E-7 | 3.02 | 4.54E-11 | 4.87 |
| 320 | 2.11E-8 | 2.96 | 2.12E-12 | 4.42 |
| 640 | 2.94E-9 | 2.84 | 1.73E-13 | 3.62 |

Table 4: Example 4.1: Numerical errors (in $l^1$ norm) and convergence rates at $t=0.1$ for GKS4 with $\alpha=2$ as well as GKS3 with $\alpha=1$.

| $N$ | GKS3 | | GKS4 | |
|---|---|---|---|---|
| | $\delta_N^1$ | $R_N^1$ | $\delta_N^1$ | $R_N^1$ |
| 10 | 7.65E-4 | — | 1.12E-4 | — |
| 20 | 1.16E-4 | 2.72 | 1.55E-6 | 6.18 |
| 40 | 3.59E-5 | 1.69 | 1.42E-7 | 3.45 |
| 80 | 1.71E-5 | 1.07 | 3.00E-8 | 2.24 |
| 160 | 8.71E-6 | 0.97 | 7.44E-9 | 2.01 |
| 320 | 4.45E-6 | 0.97 | 1.87E-9 | 1.99 |
| 640 | 2.26E-6 | 0.98 | 4.69E-10 | 2.00 |

data are taken as

$$(\rho,U,P)(x,0)=\begin{cases}(3.857134,\,2.629369,\,10.33333), & x<-4,\\ (1+0.2\sin(5x),\,0,\,1), & x>-4,\end{cases}$$

which show that a Mach 3 shock wave is right-moving into a sinusoidal density field.

Fig. 1 plots the densities at $t=1.8$ in the computational domain $\Omega=[-5,5]$ and the interval $[0,2.5]$ obtained by using GKS3 ("$\circ$") and GKS4 ("$\Delta$") with 300 uniform cells. Those are compared the reference solution ("solid line") obtained by using GKS2 with a finer mesh of 10000 uniform cells. It is seen that when the shock wave interacts with the sine wave, some complex but smooth structures are generated at the left hand side of the shock wave, and GKS4 is obviously better than GKS3 in resolving are those complex structures as well as the shock wave.

**Example 4.3** (Blast wave problem)**.** The blast wave problem, originally proposed by Woodward and Colella [32], is simulated to evaluate the performance of the high-order scheme GKS4 for the flow with strong discontinuities. The computational domain $\Omega$ is

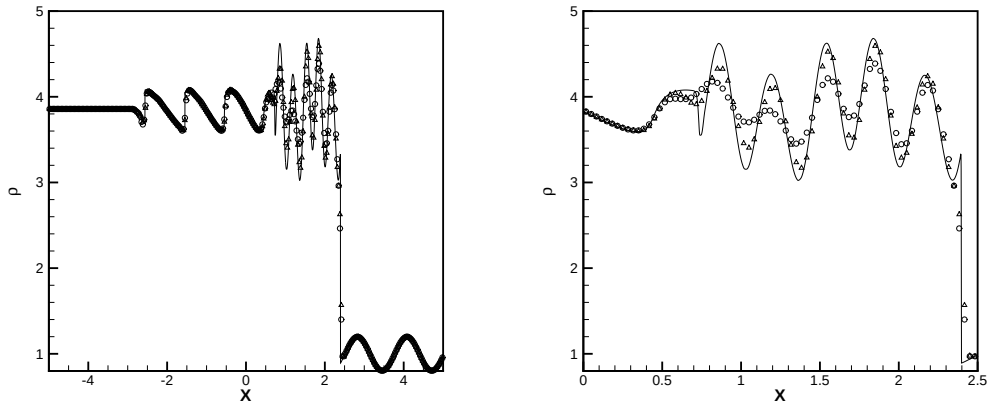


Figure 1: Example 4.2: The densities at $t=1.8$ obtained by GKS3 ("$\circ$") and GKS4 ("$\Delta$") with 300 uniform cells. The right plot is close-up of the left within the interval $[0,2.5]$.

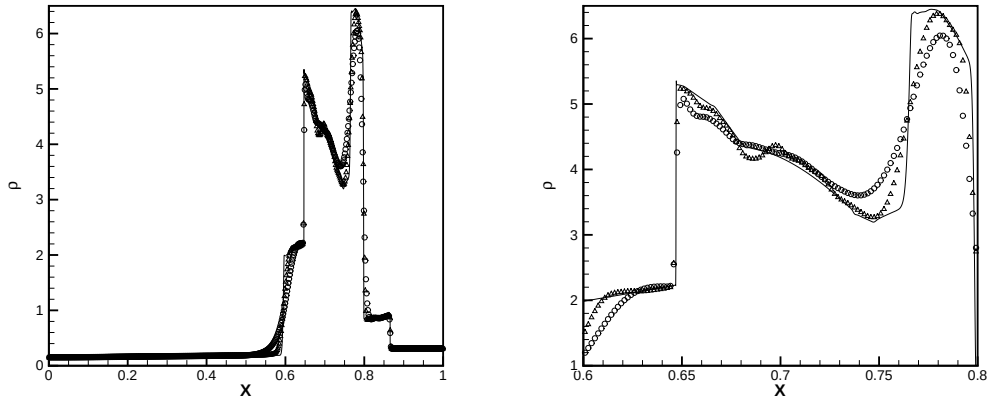


Figure 2: Example 4.3: The densities at $t=0.038$ obtained by GKS3 ("$\circ$") and GKS4 ("$\Delta$") with 600 uniform cells. The right plot is the close-up of the left within the interval $[0.6,0.8]$.

$[0,1]$ with reflecting boundary condition on both sides. The initial flow field is stationary with an unity density and the pressure is 1000 for $0<x<0.1$, 100 for $0.9<x<1$, and 0.01 between them.

The densities at $t=0.038$ shown in Fig. 2 are obtained by GKS3 and GKS4 with 600 uniform cells and compared with the reference solution ("solid line") obtained by GKS2 with a finer mesh of 10000 uniform cells. We see that with fewer grids the high order scheme GKS4 can get the same fine solution as the GKS2, and GKS4 performs better resolution in the inner structure of the blast wave.

### 4.2 2D case

Several 2D problems are considered here to test the present gas-kinetic scheme (GKS4), which is implemented by using the simple first-order accurate dimensional splitting technique (so-called Lie splitting). The first problem is for accuracy test. The followings are six inviscid problems (Riemann problems, the problem of the shock wave and bubble interaction, and the double mach reflection problem) and four viscous problems (the Couette flow, the flow near an oscillating plate, the laminar boundary layer, and the shock boundary layer problem). Unless specifically stated, the time stepsize $\Delta t_n$ is determined by the $CFL$ condition (3.1) with the $CFL$ number of 0.12.

**Example 4.4** (Accuracy test)**.** This example is used to check the accuracy of GKS4. It describes a sine wave propagating periodically at an angle of 45° relative to the $x$-axis in the domain $\Omega=[0,2]\times[0,2]$. The initial data are

$$\rho(x,y,0)=1+0.2\sin\big(\pi(x+y)\big),\quad U(x,y,0)=0.7,\quad V(x,y,0)=0.5,\quad P(x,y,0)=1,$$

and corresponding exact solutions are given by

$$\rho(x,y,t)=1+0.2\sin\big(\pi(x+y-Ut-Vt)\big),\quad U(x,y,t)=0.7,\quad V(x,y,t)=0.5,\quad P(x,y,t)=1.$$

The domain $\Omega$ is divided into $N\times N$ uniform cells and the periodic boundary conditions are specified on four boundaries. We take $\Delta t\approx\Delta x^4$ in order to realize high order in time in the present case and set the collision time $\tau$ as zero. Table 5 gives the numerical errors $\delta_N^p$ in $l^p$-norm at $t=0.1$ and corresponding convergence rates $R_N^p$ for GKS4, $p=1,2,\infty$. For comparison, Table 6 presents corresponding errors and convergence rates for GKS3. The results show that the convergence rate of 5 order may be obtained for GKS4, but the convergence rate of GKS3 is about 3. Tables 7 and 8 further give the numerical errors and corresponding convergence rates for GKS4 with $\alpha=4$ and GKS3 with $\alpha=3$, respectively. They show the same conclusion as the 1D case.

Table 5: Example 4.4: Numerical errors in $l^p$ norm and convergence rates at $t=0.1$ for GKS4 with $\tau=0$, $p=1,2,\infty$.

| $N\times N$ | $l^1$ norm | | $l^2$ norm | | $l^\infty$ norm | |
|---|---|---|---|---|---|---|
| | $\delta_N^1$ | $R_N^1$ | $\delta_N^2$ | $R_N^2$ | $\delta_N^\infty$ | $R_N^\infty$ |
| $10\times10$ | 7.20E-5 | —- | 7.99E-5 | —- | 9.39E-5 | —- |
| $20\times20$ | 2.31E-6 | 4.96 | 2.54E-6 | 4.98 | 3.04E-6 | 4.95 |
| $40\times40$ | 7.24E-8 | 4.99 | 8.00E-8 | 4.99 | 9.51E-8 | 4.99 |
| $80\times80$ | 2.28E-9 | 4.99 | 2.50E-9 | 5.00 | 2.96E-9 | 5.01 |
| $160\times160$ | 7.20E-11 | 4.98 | 7.82E-11 | 4.99 | 9.26E-11 | 4.99 |

**Example 4.5** (Riemann problem I)**.** In the following we will solve several Riemann problems of the 2D Euler equations, see [13], in which the initial data consist of four constant

Table 6: Example 4.4: Numerical errors in $l^p$ norm and convergence rates at $t=0.1$ for GKS3 with $\tau=0$, $p=1,2,\infty$.

| $N\times N$ | $l^1$ norm | | $l^2$ norm | | $l^\infty$ norm | |
|---|---|---|---|---|---|---|
| | $\delta_N^1$ | $R_N^1$ | $\delta_N^2$ | $R_N^2$ | $\delta_N^\infty$ | $R_N^\infty$ |
| $10\times10$ | 1.12E-3 | — | 1.23E-3 | — | 1.54E-3 | — |
| $20\times20$ | 1.30E-4 | 3.10 | 1.41E-4 | 3.12 | 1.66E-4 | 3.21 |
| $40\times40$ | 1.75E-5 | 2.89 | 1.83E-5 | 2.95 | 2.15E-5 | 2.95 |
| $80\times80$ | 2.18E-6 | 3.01 | 2.42E-6 | 2.92 | 5.81E-6 | 1.88 |
| $160\times160$ | 2.74E-7 | 2.99 | 3.12E-7 | 2.96 | 9.70E-7 | 2.58 |

Table 7: Example 4.4: Numerical errors in $l^p$ norm and convergence rates at $t=0.1$ for GKS4 with $\alpha=4$, $p=1,2,\infty$.

| $N\times N$ | $l^1$ norm | | $l^2$ norm | | $l^\infty$ norm | |
|---|---|---|---|---|---|---|
| | $\delta_N^1$ | $R_N^1$ | $\delta_N^2$ | $R_N^2$ | $\delta_N^\infty$ | $R_N^\infty$ |
| $10\times10$ | 7.03E-5 | —- | 7.96E-5 | —- | 9.29E-5 | —- |
| $20\times20$ | 2.34E-6 | 4.91 | 2.58E-6 | 4.95 | 3.09E-6 | 4.91 |
| $40\times40$ | 7.35E-8 | 4.99 | 8.11E-8 | 4.99 | 9.67E-8 | 5.00 |
| $80\times80$ | 2.31E-9 | 4.99 | 2.54E-9 | 5.00 | 3.02E-9 | 5.00 |
| $160\times160$ | 7.24E-11 | 5.00 | 7.92E-11 | 5.00 | 9.43E-11 | 5.00 |

Table 8: Example 4.4: Numerical errors in $l^p$ norm and convergence rates at $t=0.1$ for GKS3 with $\alpha=3$, $p=1,2,\infty$.

| $N\times N$ | $l^1$ norm | | $l^2$ norm | | $l^\infty$ norm | |
|---|---|---|---|---|---|---|
| | $\delta_N^1$ | $R_N^1$ | $\delta_N^2$ | $R_N^2$ | $\delta_N^\infty$ | $R_N^\infty$ |
| $10\times10$ | 1.03E-3 | — | 1.15E-3 | — | 1.54E-3 | — |
| $20\times20$ | 1.24E-4 | 3.05 | 1.32E-4 | 3.12 | 1.52E-4 | 3.34 |
| $40\times40$ | 1.65E-5 | 2.91 | 1.72E-5 | 2.94 | 2.04E-5 | 2.90 |
| $80\times80$ | 2.05E-6 | 3.01 | 2.29E-6 | 2.91 | 5.80E-6 | 1.81 |
| $160\times160$ | 2.56E-7 | 3.00 | 2.97E-7 | 2.95 | 9.59E-7 | 2.60 |

states in each of the four quadrants. The computational domain $\Omega$ is taken as $[0,1]\times[0,1]$. The initial data of the first Riemann problem are

$$(\rho,U,V,P)(x,y,0)=\begin{cases}(1.1,0,0,1.1), & x>0.5,y>0.5,\\ (0.5065,0.8939,0,0.35), & x<0.5,y>0.5,\\ (1.1,0.8939,0.8939,1.1), & x<0.5,y<0.5,\\ (0.5065,0,0.8939,0.35), & x>0.5,y<0.5,\end{cases}$$

which correspond to the case of a slow left-moving shock wave ($S_{12}^-$), a fast upper-moving

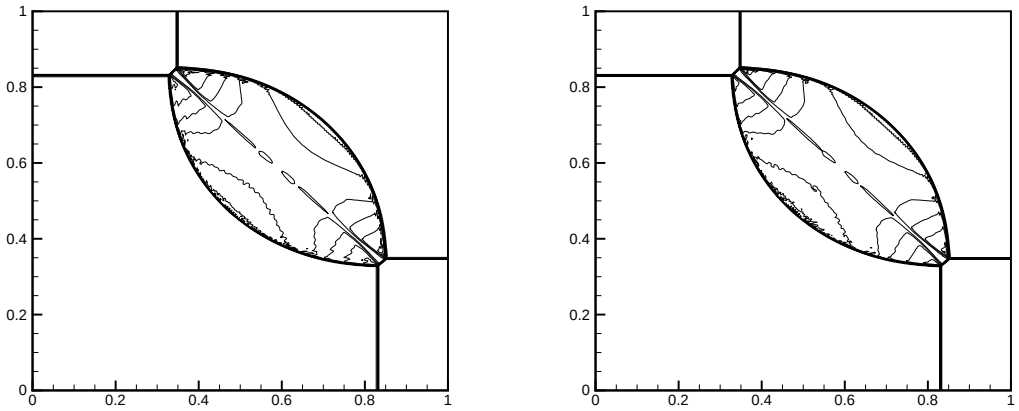


Figure 3: Example 4.5: The density $\rho$ at $t=0.2$ with 20 equally spaced contour lines ranging from 0.6 to 1.9 by GKS3 (left) and GKS4 (right) with $400\times400$ uniform cells.

shock wave ($S_{23}^{+}$), a fast right-moving shock wave ($S_{34}^{+}$), and a slow lower-moving shock wave($S_{14}^{-}$).

Fig. 3 gives the density contours with 20 equally spaced contour lines at $t=0.2$ obtained by GKS3 (left) and GKS4 (right) with $400\times400$ uniform cells. It is found that the density is symmetric with respect to the line $x=y$, and GKS4 resolve the shock waves better than GKS3.

**Example 4.6** (Riemann problem II)**.** The initial data of the second Riemann problem are

$$(\rho,U,V,P)(x,y,0)=\begin{cases}(1.5,0,0,1.5), & x>0.5,y>0.5,\\ (0.5323,1.206,0,0.3), & x<0.5,y>0.5,\\ (0.138,1.206,1.206,0.029), & x<0.5,y<0.5,\\ (0.5323,0,1.206,0.3), & x>0.5,y<0.5,\end{cases}$$

which correspond to the case of a fast left-moving shock wave ($S_{12}^{-}$), a slow lower-moving shock wave ($S_{23}^{-}$), a slow left-moving shock wave ($S_{34}^{-}$), and a fast lower-moving shock wave ($S_{14}^{-}$). It means that each of them has negative speed.

The density contours at $t=0.3$ shown in Fig. 4 are obtained by GKS4 and GKS3 with $200\times200$ uniform cells. Four initial shock waves interact each other and result in a more complicated pattern, which is symmetric with respect to the line $x=y$. The initial shock wave $S_{23}^{-}$ bifurcates at the trip point into a reflected shock wave, a Mach stem and a slip line. The reflected shock wave matches (interacts with) the shock wave $S_{12}^{-}$ to produce a new shock. It is found from Fig. 4 that GKS4 may present a better solution.

**Example 4.7** (Riemann problem III)**.** This Riemann problem is about the interaction of pure vortex sheets (contact discontinuities). Contact discontinuities are discontinuous

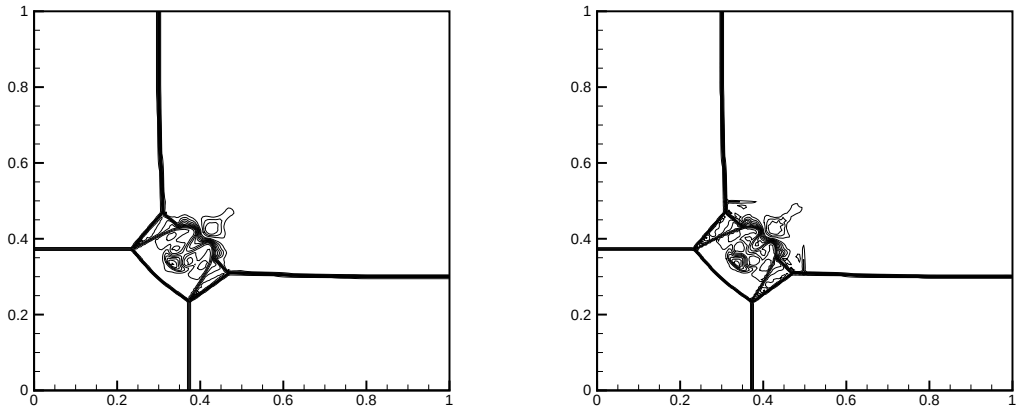


Figure 4: Example 4.6: The density contours at $t=0.3$ with 20 equally spaced contour lines ranging from 0.2 to 1.7 by GKS3 (left) and GKS4 (right) with $200\times200$ uniform cells.

surfaces on which the flow is in the pressure equilibrium, no flow moving across them. We can describe them as the surfaces across which the pressure and the normal velocity component keep continuous but the density and tangential velocity component undergo (non-zero) jump. The initial data are taken as

$$(\rho,U,V,P)(x,y,0)=\begin{cases}(1,0.75,-0.5,1), & x>0.5,y>0.5,\\ (2,0.75,0.5,1), & x<0.5,y>0.5,\\ (1,-0.75,0.5,1), & x<0.5,y<0.5,\\ (3,-0.75,-0.5,1), & x>0.5,y<0.5,\end{cases}$$

which correspond to four vortex sheets with the same sign, because the vorticity $\omega=\partial_x V(x,y,0)-\partial_y U(x,y,0)$ is less than zero across each initial discontinuity.

The densities at $t=0.23$ are plotted with 20 equally spaced contour lines in Fig. 5, obtained by GKS4 and GKS3 with $200\times200$ cells. It is found that initial contact discontinuities interact each other and a spiral is formed with the low density in the center of the domain. Both schemes can capture the important features in the interaction of four contact discontinuities, but GKS4 presents a sharper solution.

**Example 4.8** (Riemann problem IV)**.** This example is about the interaction of pure vortex sheets with different signs and totally different from Example 4.7. Specially, infinite vortices may be observed in this case when the fine mesh and high-order accurate scheme

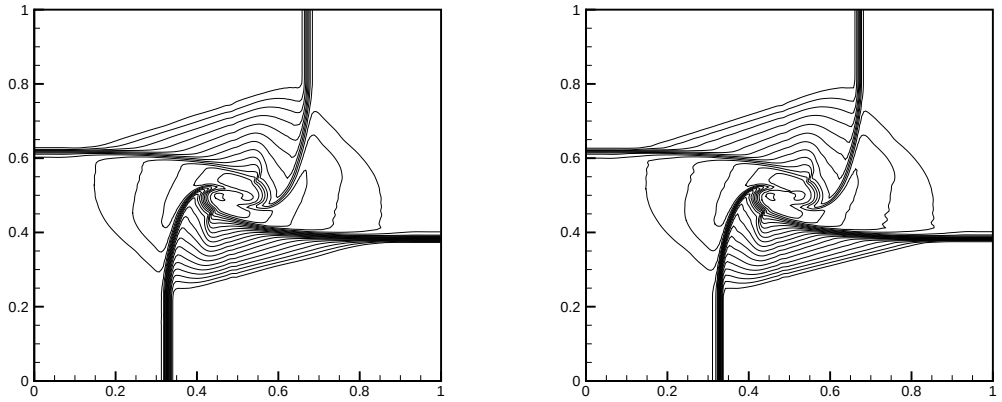

Figure 5: Example 4.7: The densities at $t=0.23$ with 20 contours ranging from 0.4 to 2.86 are obtained by GKS3 (left) and GKS4 (right) with $200\times200$ uniform cells.

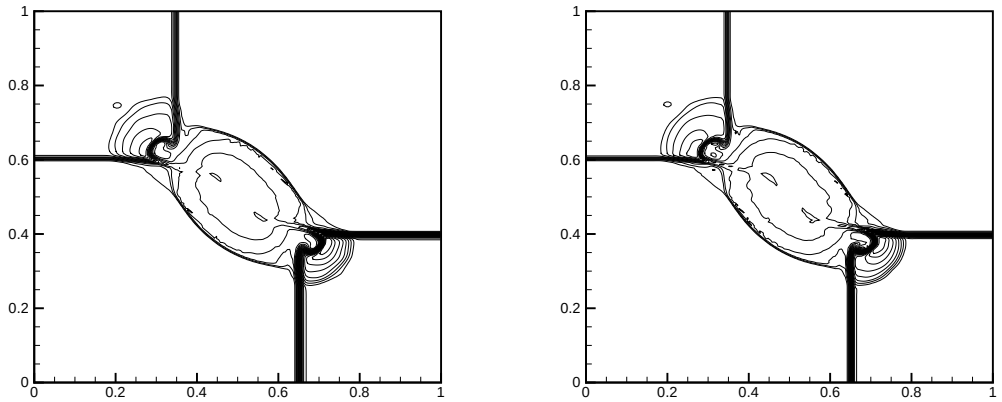

Figure 6: Example 4.8: The densities at $t=0.2$ with 25 equally space contour lines ranging from 1.2 to 3.8 are obtained by GKS3 (left) and GKS4 (right) with $200\times200$ uniform cells.

are used, see [5]. The initial data are taken as

$$(\rho,U,V,P)(x,y,0)=\begin{cases}(1,-0.75,-0.5,1), & x>0.5,y>0.5,\\ (3,0.75,-0.5,1), & x>0.5,y<0.5,\\ (1,0.75,0.5,1), & x<0.5,y<0.5,\\ (2,-0.75,0.5,1), & x<0.5,y>0.5.\end{cases}$$

The densities are plotted at $t=0.2$ with 25 equally space contour lines in Fig. 6, obtained by GKS4 and GKS3 with $200\times200$ cells. It is found that contact discontinuities are better resolved by GKS4 than GKS3.

**Example 4.9** (Double mach reflection)**.** This problem was extensively studied in Woodward and Colella [31] and later by many others, see e.g. [8,21]. We use exactly the same setup as in [21]. Initially a right-moving Mach 10 shock wave is positioned at the point $(x,y)=(1/6,0)$ and makes a $60^\circ$ angle with the $x$-axis. More precisely, the initial data within the domain $\Omega=[0,4]\times[0,1]$ are

$$\boldsymbol{W}(x,y,0)=\begin{cases} W_L, & y>h(x,0),\\ W_R, & y<h(x,0), \end{cases}$$

where $\boldsymbol{W}_L$ and $\boldsymbol{W}_R$ are the left and right states of the right-moving Mach 10 shock wave, given by

$$\boldsymbol{W}_L=(8,57.1597,-33.0012,563.544)^T,\quad \boldsymbol{W}_R=(1.4,0,0,2.5)^T,$$

and $y=h(x,t)=\sqrt{3}(x-\frac{1}{6})-20t$ is the position of the shock wave at time $t$.

A reflecting wall is placed at the $x>1/6$ part of the bottom boundary. and the state on the remainder bottom boundary, i.e., the $x<1/6$ part of the bottom boundary are set to the exact post-shock state $\boldsymbol{W}_L$. Other boundary conditions are specified as

$$\boldsymbol{W}(0,y,t)=\boldsymbol{W}_L,\quad \boldsymbol{W}(4,y,t)=\boldsymbol{W}_R,\quad 0\le y\le 1;$$
$$\boldsymbol{W}(x,1,t)=\begin{cases} \boldsymbol{W}_L, & 0\le x<x_s,\\ \boldsymbol{W}_R, & x_s<x\le 4, \end{cases}$$

where $x_s$ is the solution of the equation $h(x,t)=1$.

Fig. 7 displays close-up of the density contours with 30 equally spaced contour lines obtained by GKS3 and GKS4 with $1280\times320$ uniform cells. It is found that GKS3 and GKS4 resolve sharply shock wave, but GKS4 captures the fine details of the complicated structure around the double-Mach region much better than GKS3.

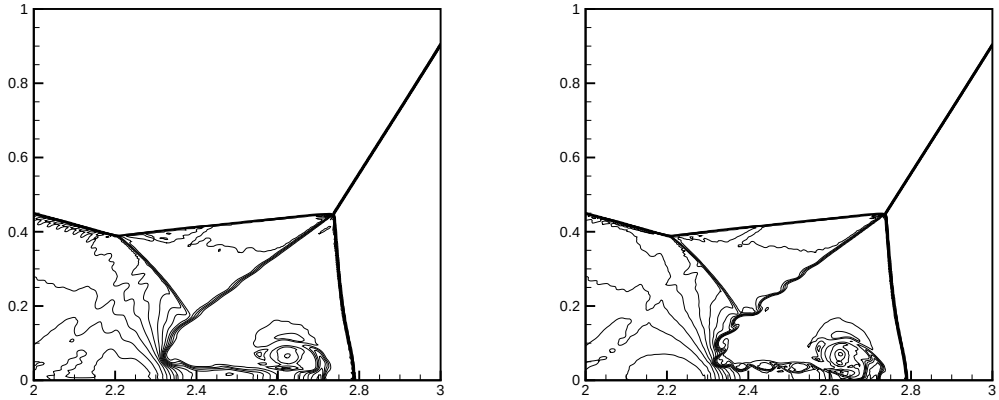


Figure 7: Example 4.9: Close-up of the density contours at $t=0.2$ with 30 equally spaced contour lines ranging from 2 to 22 are obtained by GKS3 (left) and GKS4 (right) with $1280\times320$ uniform cells.

**Example 4.10** (Shock-bubble interaction)**.** The example is to simulate the interaction between a planar shock wave and a bubble [9, 12]. The domain $\Omega$ is taken as $[-0.1,1.5]\times[-0.5,0.5]$ with reflective boundaries on the top and bottom boundaries, the inflow boundary on the left and outflow boundary at the right. Initially, the gas is at rest and has unit density and pressure. There is a bubble centered at $(0.3,0)$ with a radius of 0.2. The density inside the bubble is 0.1 while the velocities and pressure have the same values as outside. The incoming shock wave located at $x=0$ and propagates in the positive $x$-direction. The pressure behind the shock wave is 10, the other variables can be known by using the Rankine-Hugoniot jump condition.

Figs. 8-9 present the schlieren images of the density at $t=0.1,0.2,0.3,0.4$, and the clear interaction process between the shock wave and the bubble, obtained by `GKS2`, `GKS3`, `GKS4` respectively. At the beginning, the shock wave propagates in the positive direction and the bubble stay still. Then the bubble is deformed when the shock wave captures it. The shock wave penetrates the bubble and a reflected smooth wave is formed. The penetrating shock wave is speeded up inside the bubble due to the higher sound speed inside the low density region. When it hits the bubble wall, it reflects. Then two rotating vortices are formed. As time going on, more complex pattern like secondary vortices are formed. From those images in Figs. 8-9, we can see that the higher order scheme can better capture the complicate pattens appeared in the interaction process between the shock wave and the bubble.

**Example 4.11** (Couette flow)**.** Couette flow is the laminar flow of a viscous fluid in the space between two parallel plates, one of which is moving relative to the other. The flow is driven by virtue of viscous drag force acting on the fluid and the applied pressure gradient parallel to the plates. Here we assume that two infinite, parallel plates are separated by a distance $H$. The top plate translates with a constant velocity $U_0$ in its own plane. The temperatures of the lower and upper plate are given by $T_0$ and $T_1$, respectively. Both viscosity $\mu$ and heat conduction coefficient $k$ are constant.

Neglecting pressure gradients, one may simplify the Navier-Stokes equations as

$$\begin{aligned}
&\frac{d^2U}{dy^2}=0, && U(0)=0, \quad U(H)=U_0,\\
&\frac{d^2T}{dy^2}+\frac{\mu}{k}\frac{U_0^2}{H^2}=0, && T(0)=T_0, \quad T(H)=T_1.
\end{aligned}$$

and get their analytic solutions

$$\begin{aligned}
&U(y)=\frac{U_0}{H}y, \quad 0\le y\le H,\\
&\frac{T-T_0}{T_1-T_0}=\frac{y}{H}+\frac{U_0^2\mu}{2k(T_1-T_0)}\frac{y}{H}\left(1-\frac{y}{H}\right).
\end{aligned} \tag{4.2}$$

In the present study, we take $H$=1, $\rho$=1, $U_0$=1, $\mu$=$5\times10^{-3}$, $T_0$=100/1.4, $T_1$=1.0002$T_0$ and $k=\mu/\left(14.4(T_1-T_0)\right)$.

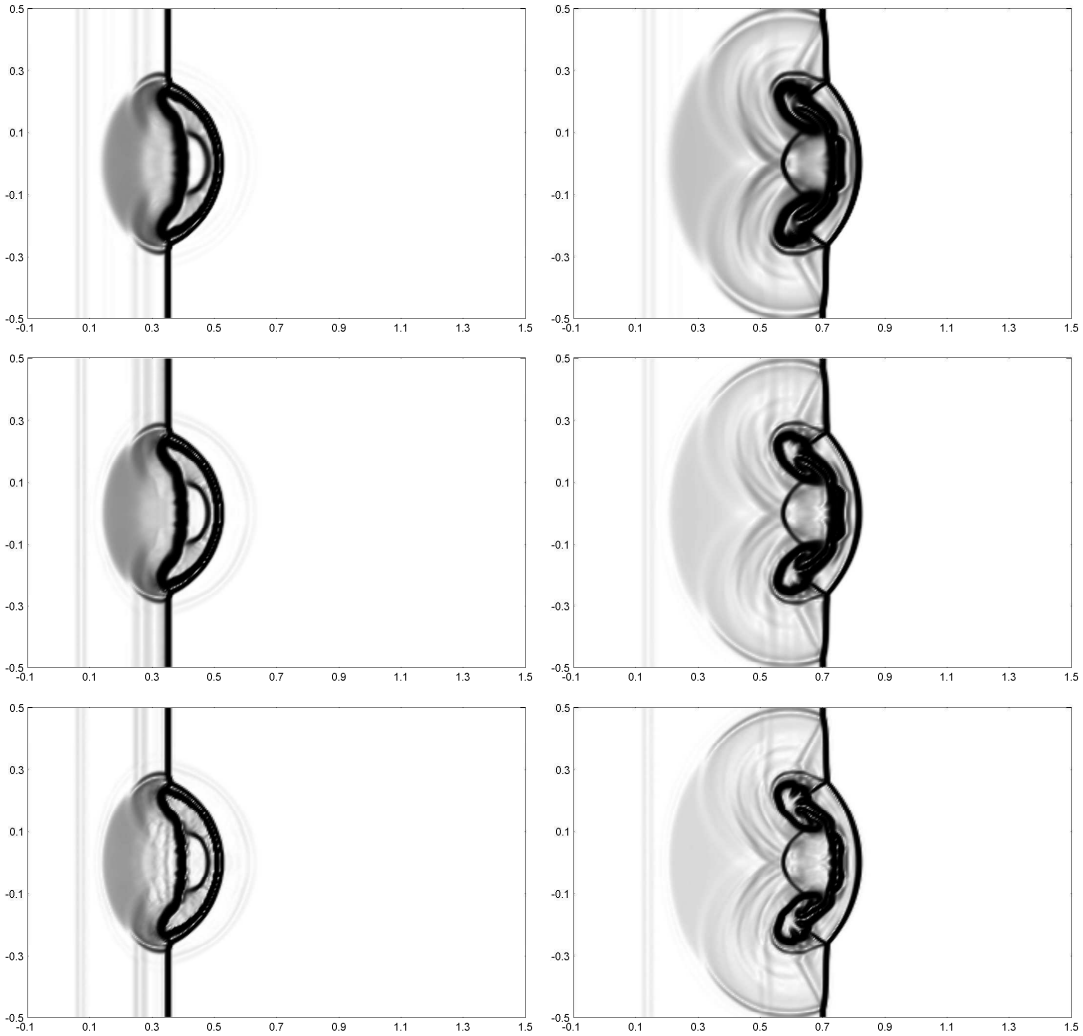

Figure 8: Example 4.10: The schlieren images of the density $\rho$ at $t=0.1$ (left) and 0.2 (right) obtained by GKS2 (top), GKS3 (middle), GKS4 (bottom) respectively with $320\times200$ cells.

Fig. 10 plots the temperature and the velocity obtained by GKS4, where the solid line denotes the analytic solution given in (4.2), the symbols '$\circ$' and '$\triangle$' denote the solutions obtained with 5 and 10 cells, respectively. We see that numerical solutions obtained by GKS4 with only a few cells are well comparable with the analytic ones. Fig. 11 gives a comparison of the temperatures obtained by using GKS4 and GKS3 with 5 cells.

**Example 4.12** (Flow near an oscillating plate)**.** This example is to consider an oscillating plate in a viscous fluid at rest with the oscillation direction(s) parallel to the plate. Harmonic motion, parallel to a plane rigid plate, will result in the fluid near the plate being dragged with the plate and forming the Stokes boundary layer (or oscillatory boundary

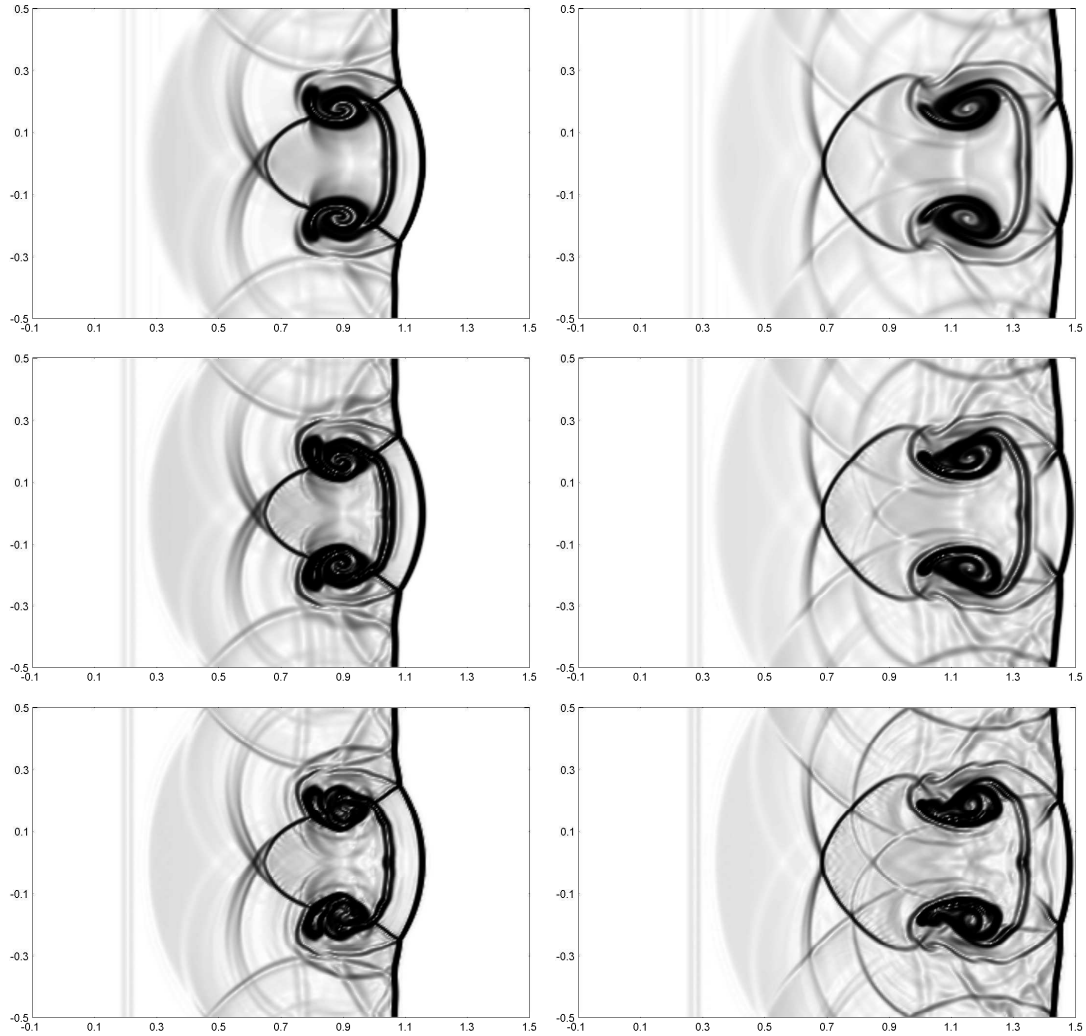

Figure 9: Same as Fig. 8 except for at $t=0.3$ (left) and 0.4 (right).

layer) close to the plate, due to the viscous shear stresses.

Suppose the motion of the plate, located horizontally in the plane $y=0$, is

$$U_{\text{plate}}(t)=U_0\cos(\omega t), \tag{4.3}$$

where $U_0$ denotes the velocity amplitude of the plate motion and $\omega$ is the angular frequency of the motion. The plate forces the viscous fluid adjacent to have the same velocity $U(y,t)$ resulting in the no-slip condition at $y=0$: $U(0,t)=U_{\text{plate}}(t)$. Far away from the plate, for $y\to\infty$, the velocity $U(y,t)$ approaches zero. Since the pressure gradient is only a function of time $t$ and not of $y$, it is zero at infinity and has to be zero everywhere. Thus

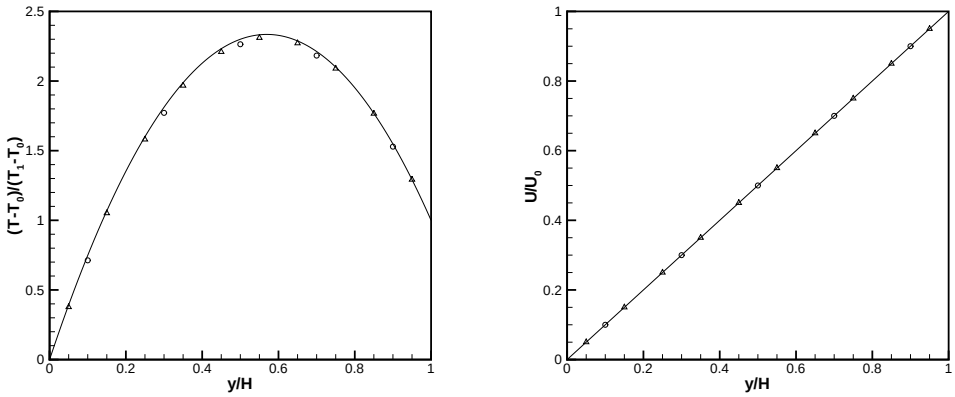


Figure 10: Example 4.11: The temperature and velocity are obtained by GKS4 with 5 cells ('○') and 10 cells ('△'), respectively. The solid lines represent the exact solutions.

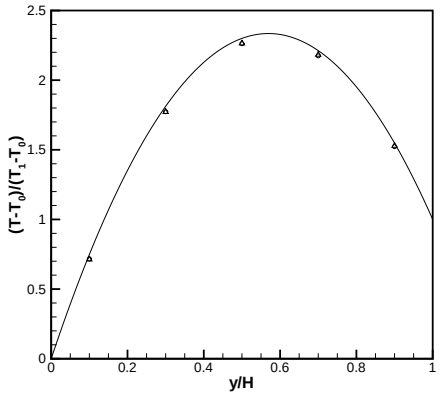


Figure 11: Example 4.11: The temperatures are obtained by GKS4 ('△') and GKS3 ('○') schemes with 5 cells, respectively.

parallel flow above the plate is governed by the equation

$$\frac{\partial U}{\partial t}=\nu\frac{\partial^2 U}{\partial y^2},$$

whose solution is

$$U(y,t)=U_0\exp(-ky)\cos(\omega t-ky), \tag{4.4}$$

with $k=\sqrt{\omega/(2\nu)}$. Here, $k$ is a kind of wavenumber in the $y$-direction, associated with a length $\delta=2\pi/k=2\pi\sqrt{2\nu/\omega}$, which is called the Stokes boundary-layer thickness. At a distance $\delta$ from the plate, the velocity amplitude has been reduced to $e^{-2\pi}\approx 0.002$ times its value $U_0$ at the plate surface. Further, as can be seen from the phase changes $\omega t-ky$

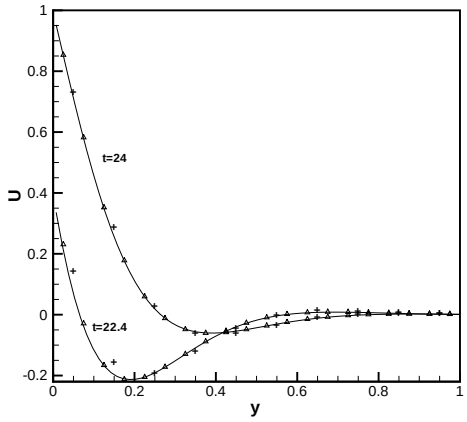


Figure 12: Example 4.12: The velocities in the interval [0,1] at $t=22.4$ and 24 by GKS4 with 30 and 60 cells respectively are compared with the analytical one ('solid line').

in the solution $U(y,t)$, the velocity oscillations propagate as a damped wave away from the wall, with wavelength $\delta$ and phase speed $\omega/k$.

In our computations, we take $\rho=1$, $P=1/(\gamma Ma^2)$, $Ma=0.1$, $U_0=1$, $\nu=\mu/\rho=0.01$, $\omega=8\pi^2\nu$ and $\gamma=5/3$. The computational domain$\Omega$ is chosen as $[0,3]$ and the velocity at the right boundary $y=3$ is specified as the analytic solution (4.4).

Fig. 12 shows the velocities in the interval $[0,1]$ at $t=22.4$ and 24 calculated by GKS4 with 30 cells ('+') and 60 cells ('$\Delta$') respectively. Fig. 13 gives a comparison of the velocities at $t=22.4$ and 24 obtained by using GKS4 and GKS3 with 30 cells in the interval $[0,1]$. We see that good mesh convergence is achieved for GKS4, and GKS4 is well comparable with GKS3.

**Example 4.13** (Laminar boundary layer)**.** We now use GKS4 to test the 2D incompressible flow of constant viscosity past a flat plate of length $L$ located horizontally. The key of such flow is the thin layer of fluid in the immediate vicinity of the plate where the effects of viscosity are significant. It is well-known that there exists the similarity solution (i.e. the so-called Blasius solution) near an attached flat plate held in an oncoming unidirectional flow.

In our computations, we take $L=100$, $\nu=10^{-3}$, and the macroscopic variables for the free stream

$$\rho_\infty=1,\quad U_\infty=1,\quad V_\infty=0,\quad P_\infty=1/\gamma Ma^2,$$

where $Ma=0.15$. The computational domain $\Omega=[-48.7,100]\times[0,82.73]$ is divided into a nonuniform rectangular mesh with $120\times30$ nonuniform cells, see Fig. 14, in which the smallest edge lengths in $x$- and $y$-directions are 0.1 and 0.07, respectively. The plate $\{y=0,x\geq0\}$ is assumed to be adiabatic and the fluid flow is non-slip on the plate. The symmetry condition is imposed at the bottom boundary $\{y=0,x<0\}$. The outflow bound-

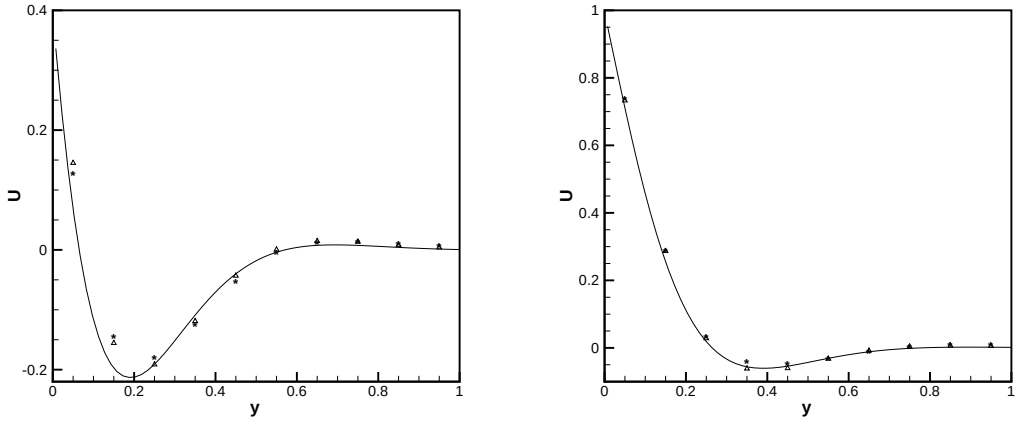


Figure 13: Example 4.12: The vertical velocities at $t=22.4$ (left) and 24 (right) are obtained by GKS3 ('$\star$') and GKS4 ('$\Delta$') with 30 cells. The solid line denotes the analytical solution (4.4).

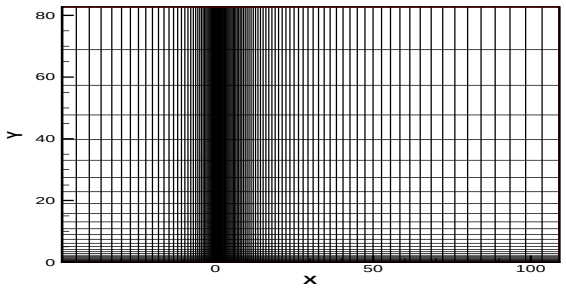


Figure 14: Example 4.13: The computational mesh with nonuniform cells.

ary condition applies to the right boundary. The other boundaries are non-reflecting and numerically treated with the Riemann invariants.

Fig. 15 displays close-up of the scaled streamwise and transverse velocities $U^*$ and $V^*$ at the location $x_O=56.988$ in the interval $[0,8]$ of $y^*$, obtained respectively by GKS4 ('$\triangle$') and GKS3 ('$\circ$'), where $U^*=U/U_\infty$, $V^*=V/\sqrt{\nu U_\infty/x_O}$, and $y^*=y/\sqrt{\nu x_O/U_\infty}$. The exact Blasius solutions are also plotted there in the solid line. The results show that the numerical velocities predicted by GKS4 fit the exact solutions very well.

**Example 4.14** (Shock boundary layer interaction)**.** This is about the interaction of an oblique shock at an angle $32.6^\circ$ with a boundary layer on the flat plate located at $\{y=0, x\geq 0\}$. The oblique shock intersects the plate at the point $(10,0)$. The Mach number of the shock wave is 2, the Reynolds number for the upstream flow is $2.96\times 10^5$, the Prandtl number is 0.72, and the dynamical viscosity $\mu$ used here satisfies the Sutherland law. The computational domain $\Omega=[-1.32,16.1]\times[0,7.78]$ is divided into a rectangular mesh

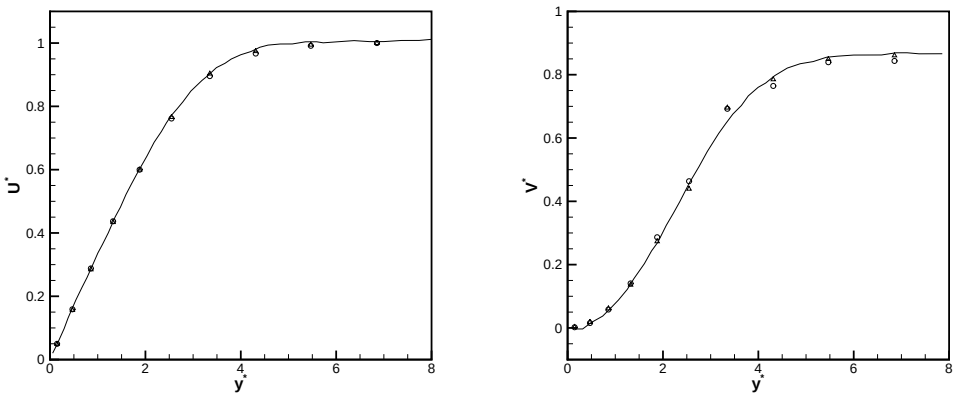


Figure 15: Example 4.13: Close-up of the streamwise and transverse velocities at $x_0 = 56.988$ in the interval $[0,8]$ of $y^*$ are obtained by GKS4 ('△') and GKS3 ('○') with $120\times 30$ nonuniform cells.

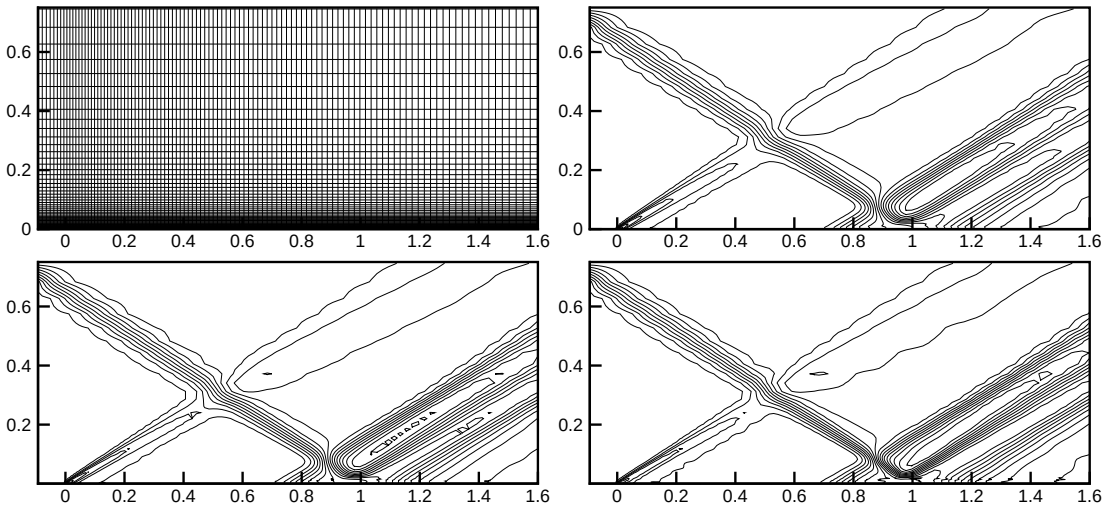

Figure 16: Example 4.14: Computational mesh with $110\times 60$ cells and the pressure contours $t = 200$ obtained by GKS2, GKS3, and GKS4, respectively. Both coordinate axes are scaled as $x/x_s$ and $y/x_s$, where $x_s = 10$.

mesh with $110\times 60$ nonuniform cells, see the fist plot in Fig. 16. The plate $\{y = 0, x \geq 0\}$ is assumed to be adiabatic and the fluid flow is non-slip on the plate.

Fig. 16 also shows the pressure contours at $t = 200$ obtained by GKS2, GKS3, and GKS4 respectively in the whole computational domain. The skin friction and pressure distributions on the plate are shown in Fig. 17, where the data '□' is the experimental data from [4]. We see that the boundary layer and the shock wave as well as their interaction are well resolved by GKS4.

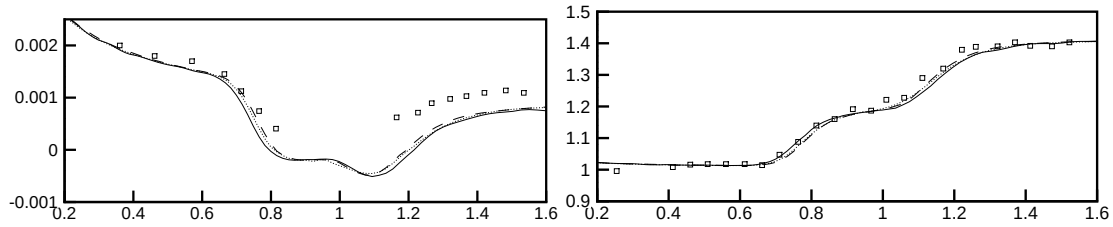


Figure 17: Example 4.14: The skin frictions (left) and the pressures (right) at $t=200$ along the flat plate are obtained by GKS2 ('dotted line'), GKS3 ('dash line'), and GKS4 ('solid line') with $110\times 60$ cells, and from the experimental data ('□'), respectively.

# 5 Conclusions

This paper developed a high-order accurate gas-kinetic scheme in the framework of the finite volume method for simulating the one- and two-dimensional fluid flows, which is an extension of the second- and third-order accurate gas-kinetic scheme. It was formed by two parts: quartic polynomial reconstruction of the macroscopic variables and fourth-order accurate flux evolution. The first part reconstructed a piecewise cell-center based quartic polynomial and a cell-vertex based quartic polynomial according to the "initial" cell average approximation of macroscopic variables to recover locally the non-equilibrium and equilibrium single particle velocity distribution functions around the cell interface. The generalized moment limiter was employed there to suppress the possible numerical oscillation. The second part evolved the macroscopic flux at the cell interface in fourth-order accuracy by means of the simple particle transport mechanism in the microscopic level, i.e. free transport and the Bhatnagar-Gross-Krook (BGK) collisions. In other words, the fourth-order flux evolution is based on the solution (i.e. the particle velocity distribution function) of the BGK model for the Boltzmann equation.

Several 1D and 2D test problems were numerically solved using the proposed high-order accurate gas-kinetic scheme, which was also compared with the exact solutions or the numerical solutions obtained the second-order or third-order accurate gas-kinetic scheme. The computations demonstrated that our scheme was effective and accurate for simulating invisid and viscous fluid flows.

# Acknowledgments

The work was partially supported by the National Natural Science Foundation of China (grant numbers: 10925101 and 91330205).

### References

[1] R. Biswas, K.D. Devine, and J.E. Flaherty. Parallel, adaptive finite element methods for conservation laws. *Appl. Numer. Math.*, 14:255–283, 1994.

[2] B. Cockburn, G.E. Karniadakis, and C.-W. Shu. *Discontinuous Galerkin Methods: Theory, Computation and Applications*. Springer, 2000.
[3] S.K. Godunov. A finite-difference method for the numerical computation of discontinuous solutions of the equations of fluid dynamics. *Mat. Sb.*, 47:271–306, 1959.
[4] R. J. Hakkinen, I. Greber, L. Trilling, and S. S. Abarbanel. The interaction of an oblique shock wave with a laminar boundary layer. *NASA, Memo 2-18-59W*, 1959.
[5] EE Han, J.Q. Li, and H.Z. Tang. Accuracy of the adaptive GRP scheme and the simulation of 2-D Riemann problems for compressible Euler equations. *Commun. Comput. Phys.*, 10:577–606, 2011.
[6] A. Harten. High resolution schemes for hyperbolic conservation laws. *J. Comput. Phys.*, 49:357–393, 1983.
[7] A. Harten, B. Engquist, S. Osher, and S.R. Chakravarthy. Uniformly high order accurate essentially non-oscillatory schemes. *J. Comput. Phys.*, 71:231–303, 1987.
[8] P. He and H.Z. Tang. An adaptive moving mesh method for two-dimensional relativistic hydrodynamics. *Commun. Comput. Phys.*, 11:114–146, 2012.
[9] H. Holden, K.A. Lie, and N.H. Risebro. An unconditionally stable method for the Euler equations. *J. Comput. Phys.*, 150:76–96, 1999.
[10] M.N. Kogan. *Rarefied Gas Dynamics*. Plenum Press, New York, 1969.
[11] L. Krivodonova. Limiters for high-order discontinuous Galerkin methods. *J. Comput. Phys.*, 226:879–896, 2007.
[12] J.O. Langseth and R.J. LeVeque. A wave propagation method for three-dimensional hyperbolic conservation laws. *J. Comput. Phys.*, 165:126–166, 2000.
[13] P.D. Lax and X.D. Liu. Solution of two-dimensional Riemann problem of gas dynamics by positive schemes. *SIAM J. Sci. Comput.*, 19:319–340, 1998.
[14] R.J. LeVeque. *Finite Volume Methods for Hyperbolic Problems*. Cambridge University Press, 2009.
[15] Q.B. Li, K. Xu, and S. Fu. A high-order gas-kinetic Navier-Stokes flow solver. *J. Comput. Phys.*, 229(19):6715–6731, 2010.
[16] X.D. Liu, S. Osher, and T. Chan. Weighted essentially non-oscillatory schemes. *J. Comput. Phys.*, 115:200–212, 1994.
[17] Y. Liu, M. Vinokur, and Z.J. Wang. Spectral difference method for unstructured grids I: Basic formulation. *J. Comput. Phys.*, 216:780–801, 2006.
[18] J.C. Mandal and S.M. Despande. Kinetic flux vector splitting for the Euler equations. *Comput. & Fluids*, 23:447–478, 1994.
[19] C.-W. Shu. High order weighted essentially nonoscillatory schemes for convection dominated problems. *SIAM Rev.*, 51(1):82–126, 2009.
[20] C.-W. Shu and S. Osher. Efficient implementation of essentially non-oscillatory shock-capturing schemes, II. *J. Comput. Phys.*, 83:32–78, 1989.
[21] H.Z. Tang and T. Tang. Adaptive mesh methods for one- and two-dimensional hyperbolic conservation laws. *SIAM J. Numer. Anal.*, 41:487–515, 2003.
[22] H.Z. Tang and H.M. Wu. High resolution KFVS finite volume methods and its applications in CFDs. *Chinese J. Numer. Math. Appl.*, 21:93–103, 1999.
[23] H.Z. Tang and H.M. Wu. Kinetic flux vector splitting for radiation hydrodynamical equations. *Comput. & Fluids*, 29:917–934, 2000.
[24] H.Z. Tang and K. Xu. A high-order gas-kinetic method for multidimensional ideal magnetohydrodynamics. *J. Comput. Phys.*, 165:69–88, 2000.
[25] H.Z. Tang and K. Xu. On positivity of a class of flux-vector splitting methods I. Explicit

difference schemes. *Math. Num. Sin.*, 23:469–476, 2001.
[26] T. Tang and K. Xu. Gas-kinetic schemes for the compressible Euler equations: Positivity-preserving analysis. *Z. Angew. Math. Phys.*, 50:258–281, 1999.
[27] E.F. Toro. *Riemann Solvers and Numerical Methods for Fluid Dynamics*. Springer, 3rd edition, 2009.
[28] B. van Leer. Towards the ultimate conservative difference scheme V: a second order sequel to Godunov's method. *J. Comput. Phys.*, 32:101–136, 1979.
[29] B. van Leer. Upwind and high-resolution methods for compressible flow: From donor cell to residual-distribution schemes. *Commun. Comput. Phys.*, 1:192–206, 2006.
[30] Z.J. Wang. Spectral (finite) volume method for conservation laws on unstructured grids: basic formulation. *J. Comput. Phys.*, 178:210–251, 2002.
[31] P. Woodward and P. Colella. Numerical simulations of two-dimensional fluid flow with strong shocks. *J. Comput. Phys.*, 54:115–173, 1984.
[32] P. Woodward and P. Colella. The piecewise parabolic method (PPM) for gas-dynamical simulations. *J. Comput. Phys.*, 54:174–201, 1984.
[33] K. Xu. Gas-kinetic schemes for unsteady compressible flow simulations. Technical Report 1998-03, VKI for Fluid Dynamics Lecture Series, 1998.
[34] K. Xu. A gas-kinetic BGK scheme for the Navier-Stokes equations and its connection with artificial dissipation and Godunov method. *J. Comput. Phys.*, 171:289–335, 2001.
[35] M. Yang and Z.J. Wang. A parameter-free generalized moment limiter for high-order methods on unstructured grids. *Adv. Appl. Math. Mech.*, 1:451–480, 2009.